Fall 2017

Solar Irradiance Forecasting and Implications for Domestic Electric Water Heating

Christopher Nutter

SOLAR IRRADIANCE FORECASTING AND IMPLICATIONS FOR DOMESTIC ELECTRIC WATER HEATING

by

CHRISTOPHER NUTTER

(Under the Direction of David Calamas)

ABSTRACT

Due to increasing concerns associated with climate change and global warming there has been a renewed interest in renewable energy resources. As most of the power production in the United States stems from the use of fossil fuels, it is desirable to pursue alternative power production avenues. For example, within the home, the domestic electrical water heater accounts for approximately seventeen percent of its total energy consumption. Reducing the amount of energy required to produce hot water from this thermal system alone can have a significant effect on reducing its carbon footprint. In this work, a modeled domestic electrical water heater was supplied photovoltaic and on-grid electrical power to increase its energy efficiency. As photovoltaic energy is directly related to solar irradiation, it is important to receive accurate solar irradiance data for the area and to forecast future solar irradiance availability. As such, a solar irradiance monitoring station, with Baseline Surface Radiation Network level performance was installed locally. Based on this real-time local data, future solar irradiance data was predicted via an artificial neural network method. If solar irradiance data can be predicted accurately then so can future photovoltaic output. It was found that local irradiance data could be accurately predicted and incorporated in a model to predict photovoltaic power output. As the photovoltaic

power output could be predicted, so could the energy savings of a domestic electric water heater operating both on-grid and on photovoltaic power.

INDEX WORDS: Artificial Neural Network, NAR, NARX, Domestic Electric Water Heat, Solar Irradiance Forecasting, Solar Energy, Thesis, College of Graduate Studies, Georgia Southern University

SOLAR IRRADIANCE FORECASTING AND IMPLICATIONS FOR DOMESTIC ELECTRIC WATER HEATING

by

CHRISTOPHER NUTTER

B.S., Georgia Southern University, 2015

A Thesis Submitted to the Graduate Faculty of Georgia Southern University in

Partial Fulfillment of the Requirements for the Degree

MASTER OF SCIENCE

STATESBORO, GEORGIA

SOLAR IRRADIANCE FORECASTING AND IMPLICATIONS FOR DOMESTIC ELECTRIC WATER HEATING

by

CHRISTOPHER NUTTER

Major Professor:	David Calamas
Committee:	Biswanath Samanta
	Mosfequr Rahman

Electronic Version Approved:

December 2017

DEDICATION

To my family and friends for their continued and valued support, especially my loving parents.

ACKNOWLEDGEMENTS

I would like to thank my advising professor at Georgia Southern University, Dr. David Calamas, for offering me this opportunity and providing his professional and academic guidance on this research work. I would like to thank Dr. Biswanath Samanta for providing his assistance regarding his expertise in MATLAB methodologies. I would like to thank Kipp & Zonen Sales Office Director, Victor Cassella, for his support regarding the purchasing, local installation, and configuration of the Kipp & Zonen solar tracking equipment. I would like to thank the undergraduate students Nicole Guajardo, Robert Wray, and Mark Hammond for their participation in solar tracking equipment installation and contributions to solar irradiance forecasting techniques.

TABLE OF CONTENTS

LIST OF TABLES

LIST OF FIGURES

CHAPTER 1: INTRODUCTION

Background

There are many parallel factors that accompany the consumption of fossil fuels. One of the most notable is the environmental consequences that are a result of the world's most used energy source. In the United States, fossil fuels account for 81% of the total energy consumption. Consisting of the burning of coal, petroleum, and natural gas consumption: the usage of fossil fuels and their role in global climate change figure prominently in the contemporary environmental and energy debates [1]. Amongst the debate is, what are the major environmental effects of burning fossil fuels and what applications are contributing to the majority of its use?

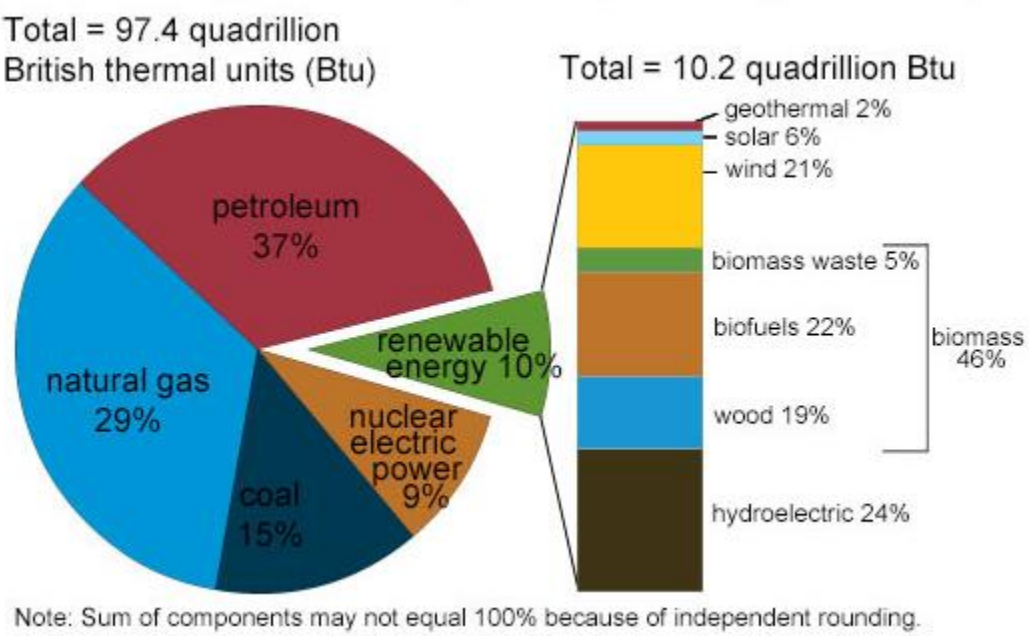

Figure 1: U.S. Energy Consumption by Energy Source in 2016 [2]

The burning of fossil fuels has been studied to show that it is a major contributor to our global warming concerns. As an effect of global warming, the average global sea level has increased eight inches since 1880. Also, it is increasing flooding risks to low-lying communities and high-

risk coastal properties whose development has been encouraged by today's flood insurance system [3]. Not only do the effects come from the burning of fossil fuels, but their extraction has had an impact as well. The processes of extraction can cause water contamination, oil spills, landform depletion, and many more contributing factors.

The use of fossil fuel has become so wide spread, because it is one of our most accessible forms of energy at the moment. These source are depleted by automotive activity, home utilities, in business, and within major cities. Within the home, water heaters account for roughly 17 percent of domestic energy use, comparatively consuming more energy than nearly all other household appliances [4]. The typical domestic water heater consists of two heating elements within the tank that are supplied power by the electrical grid to meet a home's hot water needs. The amount of power that is required to operate them can range up to 16.5 kWh per day. Therefore, increasing the energy efficiency of a home's electrical water heater can greatly diminish its effects on the environment.

Principles of Photovoltaic Power

There are many different types of alternative energy forms. Amongst the various forms of renewable energy sources, solar radiation is one of the most abundant and accessible to exploit even though solar power generation is characterized by lower power density (in terms watts per square meter) associated with the solar radiation and low conversion efficiency [5]. Solar electricity is a form of solar energy that is produced when sunlight is illuminated upon a photovoltaic solar panel. Solar electricity is also referred to as photovoltaic solar, or PV solar. Multiple solar panels can be connected in series, parallel, or a combination of both to produce a variation of output voltages and currents depending on the application of the system. This is known as a solar array. These systems can be operated as an off-grid system, which works

independently; or they can be grid-tied or grid-connected, meaning they are connected within the electrical grid.

Solar panels are able to produce electricity as the sun continuously undergoes intense nuclear activity. This activity generates large amounts of solar irradiance (W/m^2), and this generates light energy known as photons. The panels are able to produce electricity once these photons collide with the solar panel using a process known as the photovoltaic effect, a phenomenon that was observed by scientist in the 19th century. They were able to notice that certain materials produce an electric current when exposed to light. Today, the material solar panels consists of is two layers of a silicon. Silicon is relatively effective semi-conduction material and it is cut into thin wafers. These wafers are aligned together to make a solar cell and these solar cells are attached to conductive metal strips to conduct the electrical current.

Solar Irradiance Determination

Since the power output of a photovoltaic system is directly related to amount of sunlight emitted upon it, knowledge of the amount of solar irradiance is important. With the installation of a solar monitoring station, real time solar energy data can be provided for the area. The proper installation of this equipment gives accurate irradiance data. The National Renewable Energy Laboratory (NREL), the United States' only federal laboratory dedicated to the research, development, commercialization, and deployment of renewable energy and energy efficiency technologies, is the sole proprietor for providing this information. An overview of the photovoltaic resources in the United States and in Georgia can be seen in Figure 2 and Figure 3 respectively

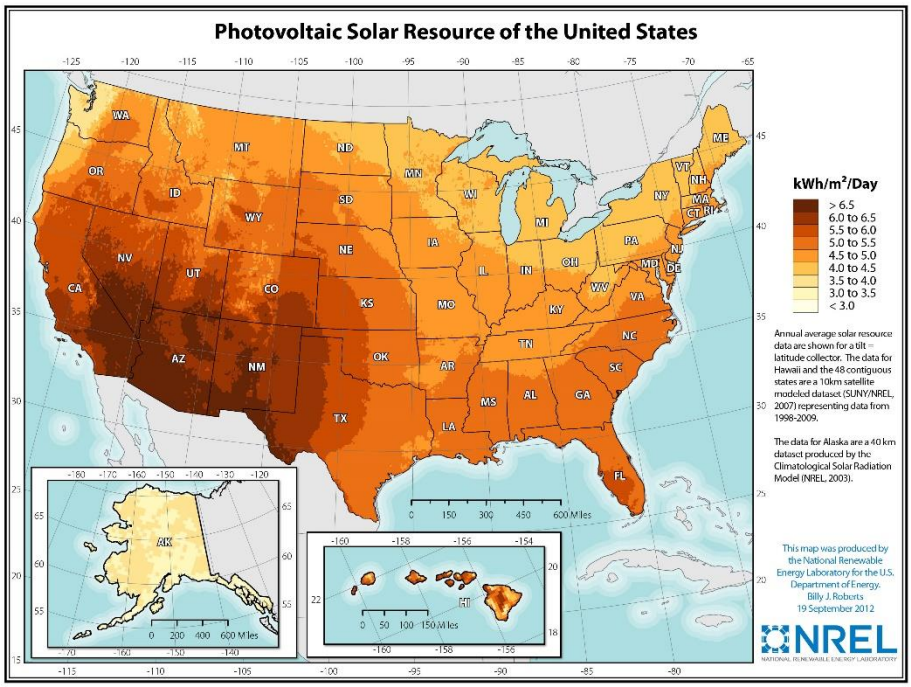

Figure 2: NREL Photovoltaic Solar Irradiance (kWh/m^2) Data per Day [6]

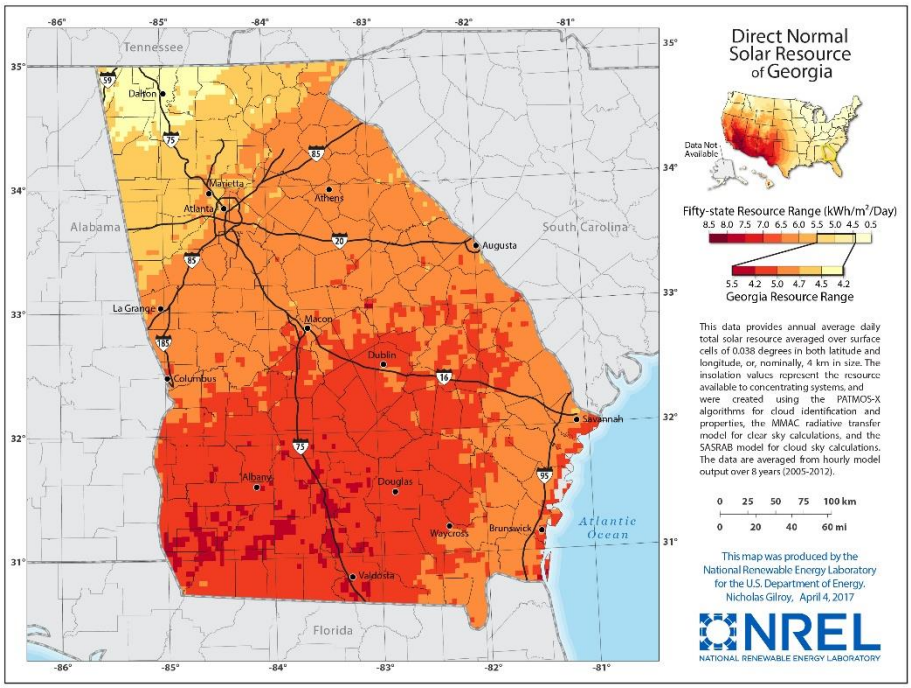

Figure 3: Direct Normal Solar Resource of Georgia [7]

Solar Tracker Background

Several manufacturers, such as Kipp & Zonen (Figure 4), develop equipment that is accurate enough to provide BSRN (Baseline Surface Radiation Network) level performance. The BSRN provides the highest quality data about solar and atmospheric radiation and the energy balance at the Earth's surface.

Figure 4: Kipp & Zonen SOLYS 2 Solar Tracker and Irradiance Equipment

In order to provide this accurate data, the tracker is usually equipped with its base, a pyrheliometer, two pyranometers (one shaded and one unshaded), and a shaded pyrgeometer. The base (Figure 5) comes equipped with GPS tracking, allowing it to determine where the sun is and follow it during sunrise to sundown. The pyrheliometer (Figure 6) is mounted alongside the base of the tracker. It is responsible for measuring the direct beam solar irradiance, and it has a field of view that is limited to 5°. This sensor points directly at the sun to provide the direct normal irradiance (DNI). There are also two pyranometers (Figure 7) mounted on top of the

tracker to retrieve short-wave irradiance data. A shaded pyranometer is a radiometer used to determine the diffused horizontal irradiance (DHI), and the unshaded pyranometer is used to measure a combination of both the diffuse and direct irradiance; denoted as the global horizontal irradiance (GHI). The shaded sensor is shaded so that it is not affect by the DNI. The system also includes a pyrgeometer (**Error! Reference source not found.**), which is a radiometer designed for measuring long-wave irradiance on a plane surface which results from radiation incident from the hemisphere above the instrument. The sensor is usually mounted on top of the tracker and it is also shaded to ensure that the results are not affected by direct irradiance.

Figure 5: SOLYS 2 Sun Tracker Base

Figure 6: Pyrheliometer Sensor

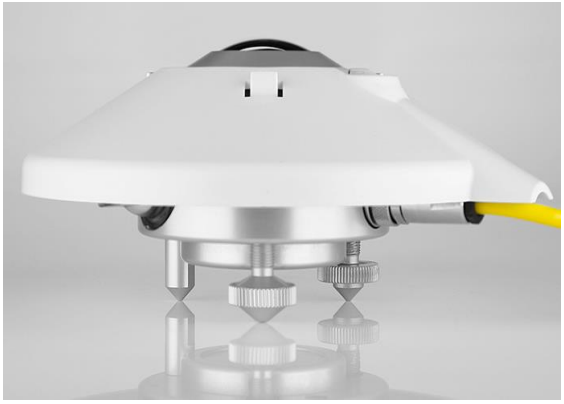

Figure 7: Pyranometer Sensor

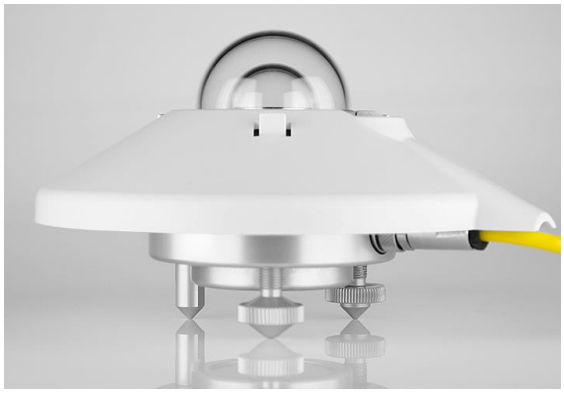

Error! Reference source not found.: Pyrgeometer Sensor

Motivation

As the efficiency of solar panels and the efforts to reduce the carbon footprint are constantly improving, it is desirable to be apply photovoltaic energy to our commonly used appliances and technology. Forecasting solar irradiance data can aid in the implementation of predictive control of a variety of technologies based on the optimal opportunity to provide efficient solar power.

Objectives

The objectives of this research were to: (1) determine proper equipment and installation to determine local solar irradiance data, (2) accumulate an abundant amount of remote solar irradiance data of BSRN level accuracy, (3) perform optimal artificial neural network methodologies to forecast the results of the remote site, (4) use local predicted solar irradiance data to determine potential local photovoltaic output, and (5) implement the PV results to domestic electric water heating to determine potential energy efficiency improvements.

CHAPTER 2: LITERATURE REVIEW

In order to determine the best option for increasing the energy efficiency of the domestic electric water heater and forecasting of solar irradiance using Artificial Neural Network (ANN) modeling, it is important to understand the concept of the system at hand. That is why it is important to be able to properly produce an ANN that provides optimal irradiance forecasting results. Also, it is essential to construct a photovoltaic (PV) model and domestic electric water heater (DEWH) model that is equal in both simplicity and accuracy, because it will serve as a representation of the physical system.

Solar Irradiance Forecasting Literature Review

There are many different methods, approaches, and procedures that can be used for prediction and forecasting of solar irradiance data. There also many studies that have focused on the improvement of these techniques. Essentially, forecasting methods that focus on historical solar irradiance data can be placed into two different categories: statistical models and numerical weather prediction (NWP) models. Statistical models are typically applied to forecast solar irradiance of a short term timescale from 5 minutes up to 6 hours. [8] These include linear (time series) models and nonlinear (artificial intelligence) models such as: artificial neural network (ANN), neuro-fuzzy network models, wavelet analysis based models, etc. [9]. NWP models are based on physical phenomenon and are used for longer forecast horizons, from about 4 to 6 hours onward [10]. The following section outlines these two different modeling approaches over time.

Short Term Solar Irradiance Forecasting

As previously stated, statistical models are typically used to predict result in the short time frame, particularly ANNs, because the NWP method is a time consuming process [11]. The statistical method is determined by the analysis of a specific amount of historical weather data in terms of predicting solar irradiance data. Several studies have used artificial intelligence (ANN and neuro-fuzzy networking) methods to produce predictions of hourly values of global horizontal irradiance by investigating other meteorological variables such as temperature, wind speed and pressure [12] [13]. Furthermore, several studies have also focused on the use and comparisons of various linear time series models.

Photovoltaic System Model Literature Review

A photovoltaic solar system is able to generate electricity based off the ambient temperature and the amount of sunlight that shines upon the solar module. Since there can be an abundant amount of sunlight within the southeastern region of the United States, solar energy has the potential to be a productive replacement of fossil fuel within the area. Therefore, it is highly important to develop several models of PV modules to determine the efficiency of the solar system [5] within its specific installation location. These models can be determined by implementing the governing equations based on the model's complexity and using the manufacture provided solar panel data sheets. That models' complexity is determined by the amount of unknown parameters and independent equations that governs the system. The main purpose of these models is to estimate non-linear current – voltage (I-V) curves, and these values are used to determine the power (watts, W) output generated by the system. There are three different models that can be used to determine the characteristics of a PV model and they consist of: one-diode model, one-diode based four-parameter model, or two-diode model. Since comparing the accuracy of these separate models is not the main purpose of this study, it is

essential to conduct an extensive literary observation of studies that have done it to determine the best option to duplicate.

One-Diode Based Five-Parameter Model Review

A one-diode PV model is a modification of an actual PV panel/module that is represented using a current source with a parallel diode and network of resistors. The model assumes that the current can be labeled by a single exponential dependence modified by the diode ideality factor [14] [15] [16]. The equivalent circuit of the one-diode PV model can be seen below in Figure 8. The model consists of current source (I_{ph}) that is directly proportional to the amount of light irradiating the module, a single diode, and a pair of resistors.

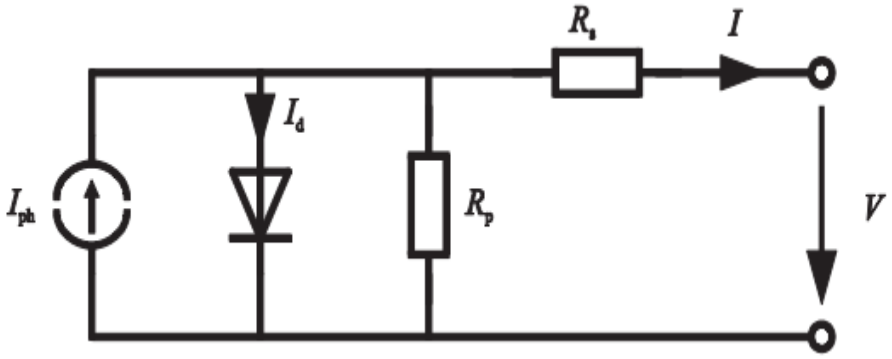

Figure 8: One-Diode Equivalent Circuit of a PV Module

In this equivalent circuit, there are five unknown parameters. They include the photocurrent (I_{ph}), the reverse saturation current (I_{sat}), (m) the diode ideality factor, the series resistance (R_s) and the shunt resistance (R_p) [14].

One-Diode Based Four-Parameter Model Review

While in Cristaldi's study, an ideal PV module is created with a current source in parallel with a diode considered with the Shockley exponential characteristic curve [5]. Known as a one-diode

based four parameter, it consist of a current source (I_{ph}) that is directly proportional to the amount of light irradiating the module. This is considered to be a simplified model of a PV panel, as it consists of single diode and a single resistor; as seen in Figure 9. As opposed to the one-diode model consisting of five unknown parameters, this model assumes that the shunt resistance is so high that it can be neglected without affecting the model characteristics drastically [14].

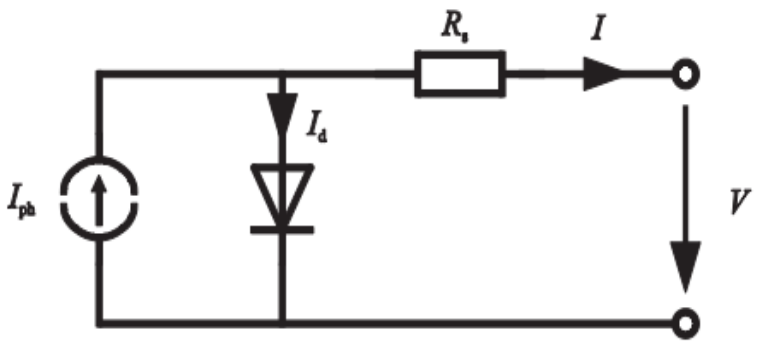

Figure 9: One-Diode/ One- Resistor Equivalent Electric Circuit of a PV Module

Since this model makes the assumption that shunt resistance can be neglected, it consists of four unknown parameters and this matches the amount of determining equations.

Two-Diode Model Review

The third model is known as the two-diode model as it consists of two diodes, a shunt resistor, and a series resistor. The second diode models the recombination losses in the depletion region [14]. Studies evaluate the two-diode model, because in a real solar cell, the recombination represents a substantial loss, which cannot be appropriately modeled using a single diode alone [17].

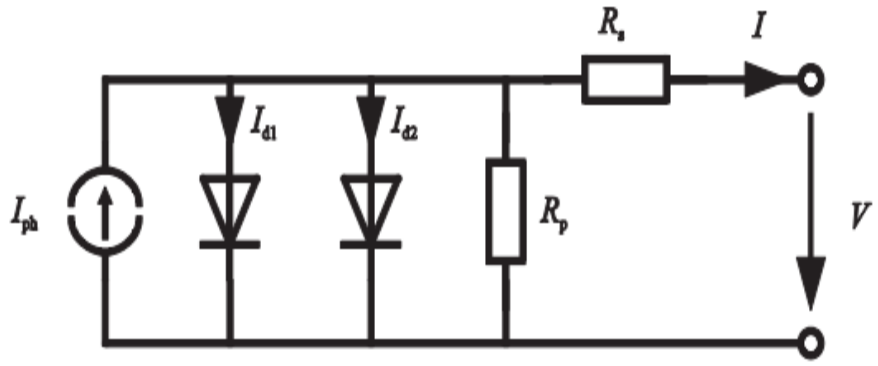

Figure 10: Two-Diode Model

The two-diode model is constructed much like the one-diode model consisting of five unknown parameters, but the second diode calls for a system that involves two more unknown parameters; resulting in a total seven unknown variables. The new parameters originate from the second diode and they include the diode reverse saturated current (I_{sat2}) and the diode factor (m_2).

Modeling of a Photovoltaic Array

Each of the three models described, evaluates the parameters at a known condition. This is known as the standard test condition (STC): it is defined as a solar irradiance of $1000\ W/m^2$ and a temperature of $25\ ℃$ [14]. These parameters are represented on datasheets that are provided by the manufacture of the PV solar panel, and they are entered within the governing equations to determine the unknown characteristics of the PV module. Once the parameters are placed into the system equations, certain assumptions can be made depending on the amount of unknown parameters.

The two-diode model is a preferable choice in terms of accuracy, but the demand for its computation requirements are considered to be much more difficult compared to single diode models. This model becomes less attractive, because there are three more unknown parameters than governing equations [17] [18]. Therefore many assumptions have to be made and if they are

incorrect, then the entire model can be invalid. The main challenge then becomes to estimate the values of all the model parameters while maintaining a reasonable computational effort [17, pp. 586-587].

As opposed to the two-diode model, the one-diode (four-parameter) model is the most simplistic of the three model types. Since the amount of unknown parameters matches that of the known governing equations, the model is much easier to compute. However, due to the simplicity of the model, it exhibits deficiencies in results when subjected to a variance in temperature [19] and it assumes that the shunt resistance is too high to effect the results of the model drastically. Even though the shunt resistance will be relatively high, accuracy of the model will be effected despite this assumption.

The one-diode (five-parameter) model is another alternative, as it is most commonly used for producing PV studies due to its accuracy [20]. It also serves as an extension of the single diode model which includes an additional shunt resistance [19].

Within the study of Taherbaneh, Farahani, and Rahmani: the main goal was to investigate the accuracy of both the one-diode (five parameter) and the two-diode models [21]. The authors utilized MATLAB Simulink to develop mathematical models to solve the governing equations simultaneously. It was hypothesized that the accuracy of the one-diode model was to be superior to that of the two-diode model. This hypothesis was proved to be incorrect as it is seen in the results of the study that the simulations are comparable with data from measurement for both models and both models have the same accuracy in the measurement range of environmental conditions [21]. Although there were discrepancies within the results of the two models, they were deemed to be miniscule and considered to have similar results. This proves that either of

the one-diode models has enough accuracy and feasibility to serve as a definitive representation of a physical photovoltaic module.

Domestic Electric Water Heater Modeling Literature Review

Principles of Heat Transfer

Thermal systems are those that involve the transfer of heat from one substance to another. Heat can flow through conduction, convection, and radiation [22]. Conduction is the transfer of heat between two solid bodies. Convection is a process in which heat is transferred between a solid surface and a liquid. An example of convection heat transfer is water heating in a pressurized vessel, as the heating of the water is due to the transfer of heat from the vessel. Radiation heat transfers occurs when two bodies are at different temperatures and separated by distance. An electric water heater utilizes the processes of both conduction and convection. The heating element is responsible for the conduction aspect and the transfer of heat within the water corresponds to the convection process.

Modeling of DEWH Review

Domestic electric water heaters (DEWH) heat domestic water in a pressurized vessel by using electric emersion heaters or elements that have a specific wattage ratting. These tanks can include one emersion heater, but they typically contain two elements for much higher demand situations. These DEWH are known as duel element water heats. The two elements are thermostatically controlled and they are wired to operate non-simultaneously. The bottom

heating element will typically operate until the desired temperature is reached, and then the top element will operate. The process is repeated depending on the demand for hot water. This increases the heat transfer of the system due to the fact that hot water rises to the top of the tank. This desired phenomenon is known as stratification. There are many works that focus on modeling the operation of a domestic electric water heater. These models can become quite complex when considering the consequences of heat transfer and stratification. Some studies have considered these parameters to model the DEWH [23] [24]. To simplify the modeling of the system, several studies have also considered a tank that was operational as a one element model, also known as a one-node model [25] [23]. These models assume that the water within the tank has uniform temperature, thus simplifying the computation of the system. Although less accurate, these models were still able to produce comparable results in relation to the more complex counterpartying multi-node models.

CHAPTER 3: RESEARCH METHODOLOGIES

Local Solar Irradiation Data Collection

In order to determine the potential efficiency of both modeled and physical photovoltaic modules, it is beneficial to be able to get an accurate set of irradiance data within the area of the of the system installation. Irradiance results can be provided for the southeastern region of Georgia, but radiometer installation and data may not be up to BSRN level. The National Renewable Energy Laboratory specializes in providing BSRN level irradiance results, but their nearest laboratory location is in Oak Ridge, Tennessee. Therefore, the installation of this equipment within the southeastern region of Georgia is desirable to obtain accurate and local solar irradiance data.

The process began with determining a location for the sun tracker: one that is clear of any shading throughout the day. After determining the installation location (Georgia Southern University Paulson Stadium press box, as seen in Figure 11), the type of radiometer equipment was selected. This project incorporated the SOLYS 2: Two-Axis Sun Tracker, which is an all-weather positioning platform used to point specialized instruments at the sun's movement across the sky. It came equipped with a GPS receiver that automatically configures location and time data, and if installed correctly it has a solar pointing accuracy of $< 0.01^{\circ}$, meeting BSRN requirements. The SOLYS 2 also came with a top mounting plate, two side plate mounts and a shading assembly. Along the side plate mount, a pyrheliometer and a sun sensor is mounted. Atop of the mounting plate, two pyranometers and a pyrgeometer was mounted. The two pyranometers and the pyrgeometer also include CVF4 Ventilation Units, which are designed to improve the reliability and accuracy of the radiometer measurement by reducing dust, raindrops,

and dew from blocking its detector. The ventilation unit operates by 12 VDC and is fully operational at up to 100% humidity.

Figure 11: Kipp & Zonen SOLYS 2 Sun Tracker installation at Georgia Southern University Paulson Stadium

On the side mount, the pyrheliometer and sun sensor (shown in Figure 12) was mounted to determine the direct irradiance and to increase the accuracy of the sun tracking ability respectively. With the sun sensor included on the sun tracker, the accuracy of the tracker increases to $< 0.05^{\circ}$ of active tracking from $< 0.01^{\circ}$ of passive tracking. The sun sensor is responsible for ensuring that the sun sensor is constantly tracking based of irradiance reading rather than strict GPS dependency. The CHP 1 pyrheliometer is a tubular shaped radiometer that specializes in determining the direct normal incidence. This radiometer has full opening view angle of $5^{\circ} \pm 0.2^{\circ}$. By limiting the view angle, this ensures that the radiometer is pointing directly at the sun while the sensor is up. The sensor also has a sensitivity of $8.06\frac{\mu V}{W/m^2}$.

Figure 12: Pyrheliometer and Sun Sensor Mounted to Side Plate of the SOLYS 2

It shown in Figure 13 that the system consisted of two CMP 10 pyranometers, which are used to measure (global and diffused) short wavelength irradiance (0.3 to 3 μm). The CMP 10 consists of one 32-junction thermopile sensing element which features quick response, improved linearity, and a wide measurement range. In order to measure diffused irradiance, the shading ball assembly was adjusted in a way to block the detector of one of the radiometers to ensure that it is not affected by direct irradiance. The second pyranometer was mounted in a way that the shading ball assembly does not cast a shadow on it. This allowed the system to produce the global irradiance, which is a combination of direct and diffuse irradiance. Both radiometers had a field of view of 180˚, the shaded pyranometer has a sensitivity of $9.04\frac{\mu V}{W/m^2}$, and the unshaded pyranometer has a sensitivity of $8.13\frac{\mu V}{W/m^2}$.

As short-wave radiation is measured by a pyranometer and the long-wave radiation by a pyrgeometer (shown in Figure 13). Long wave radiation is considered to be the far infrared

thermal energy at wavelengths from 4.5 μm to beyond 40 μm. The solar tracker was installed with a CGR 4 pyrgeometer among the top mounting plate, as it complies with the requirements of the World Meteorological Organization. The CGR 4 has a sensitivity of $11.56\frac{\mu V}{W/m^2}$.

Figure 13: Shaded Pyranometers, Un-shaded Pyranometer, and Shaded Pyrgeometer Mounted Respectively on the Top Mounting Plate of the SOLYS 2

After the installation process, each radiometer and ventilation unit was wired to LOGBOX SD data logger that is able to take up to eight analogue and four digital inputs. The data logger is configured with LoggerNet data acquisition software via RS 232 serial communication. The data logger is designed for measuring, processing, and recording of measured data in real time for the needs of meteorology and solar data utilization. Concluding the configuration of all the data, the results were provided live over a specified URL (http://141.165.72.78/) and they were readily updated by the system. The data received by the radiometers was extracted and displayed graphically.

Solar Irradiance Data Set

Since the accumulation of a substantial amount of solar irradiance and meteorological data requires a substantial amount of time, it was imperative to determine the amount of data necessary for optimal results. Historical solar and weather data from the NREL Solar Radiation Research Laboratory (SRRL): Baseline Measurement System (BMS) in Golden, Colorado was collected, because an extensive amount of historical data is made readily available and a vast majority of the equipment used in this location is of the same make and model used locally at Georgia Southern University. The forecasting of the irradiance data in Golden, Colorado was used to validate the forecasting of the local irradiance data here at Georgia Southern University, and the amount of local historical data will continually increase over time.

The data retrieved remotely (Golden, CO) consisted of the hourly mean global horizontal irradiance data, direct normal irradiance data, diffused horizontal irradiance, azimuth angle, zenith angle, cloud coverage percentage, relative humidity, and dry bulb temperature. This data was collected to determine the optimal inputs to improve the results of the artificial neural network. Similarly, hourly mean global horizontal irradiance data, direct normal irradiance data, diffused horizontal irradiance data, and dry bulb temperature can be determined locally. Since the azimuth and zenith angles represent the location relative to the sun, they can be determined by the day of the year, time of the day, and spherical coordinates. These angles were collected using a solar position calculator provided by the National Oceanic and Atmospheric Administration (NOAA).

After the data was collected, it was normalized to be within a range between zero and one. This process was done for the remote and local data sets. It was done to compare the results between the different data sets, to reduce the value of skewing results, and incorporate a stable

convergence of weights and biases. Equation 1 was used to normalize the data sets. A sample set of the normalized hourly GHI data over the span of two years (January 1, 2015 – December 21, 2016) from the NREL SRRL in Golden, Colorado can be seen in Figure 14.

$$z_i = \frac{x_i - \min(x)}{\max(x) - \min(x)} \qquad \text{Equation 1}$$

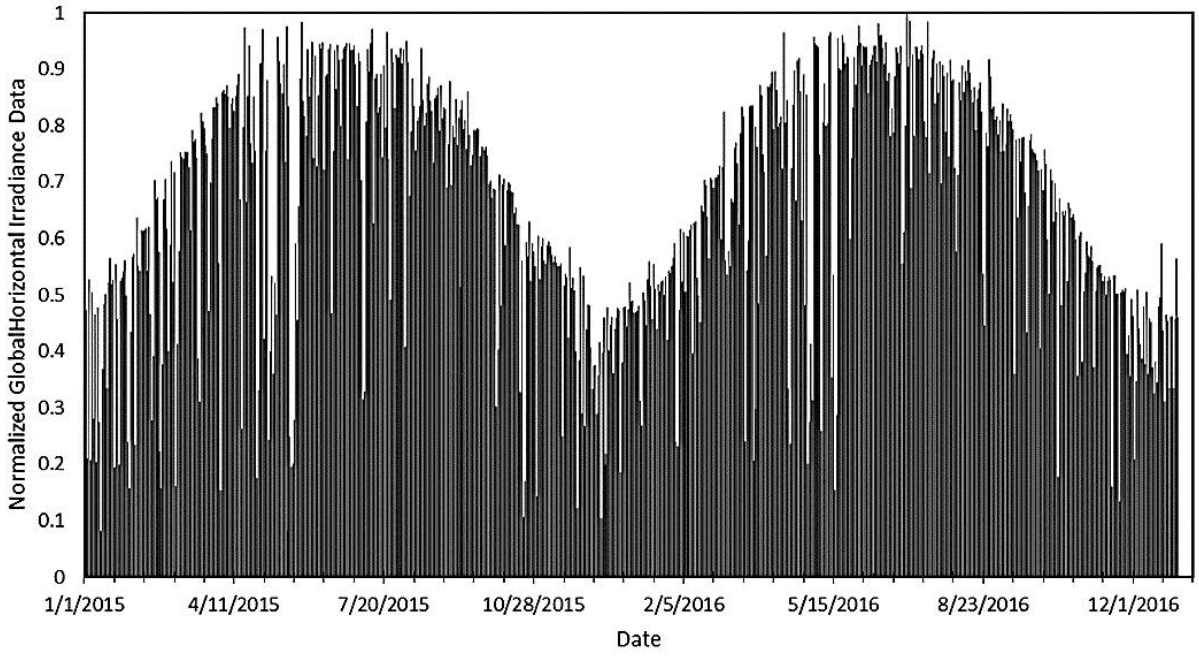

Figure 14: Global Horizontal Irradiance Time Series over Two Years (Hourly Time Steps) (Normalized Colorado Dataset [26])

Using the neural network time series tool provided by MATLAB, the average hourly global horizontal irradiance was predicted one-step ahead. This means the forecasting was set to be produced one hour ahead of the current time step. Nonlinear autoregressive (NAR) and nonlinear autoregressive with external input (NARX) models were used to determine the optimal method for predicting solar irradiance.

The Levenberg-Marquardt (LM) back propagation learning algorithm was used to evaluate the data. Seventy percent of the GHI targeted time steps were used for the training the algorithm. Within the training parameter of the data set, the network is adjusted according to its error. Fifteen percent of the data set was used for validation. The validation data sets are used to measure network generalization, and to halt the training parameter when the generalization no longer improves. This is indicated by an increase in the mean squared error (MSE) of the validation samples. The last fifteen percent of the data set was utilized for testing. These data sets provide an independent measure of the network performance during and after training, because it actually has no effect on the training parameter.

Solar Irradiation Data Forecasting

In this work, three different procedures were utilized to predict solar irradiation data. Firstly, the data was collected and normalized. Secondly, artificial neural network modeling was implemented within MATLAB neural network toolbox. Finally, the performance was of the system was analyzed. These methods were utilized for both remote and local historical data sets. It was important to determine the optimal inputs, delay parameters, and neuron numbers for the specific locations.

For the remote data set, comparisons were made between the NAR and NARX networks. NAR models are used to predict data from a one-dimensional time series, meaning the forecasted results are only determined by the output of the historical data alone. NARX models are used to predict data form a multidimensional time series and they use external information to improve the performance. So the NARX network was used to determine which inputs were needed, in terms of solar irradiance prediction, to produce optimal results. The input configurations and input parameters can be seen in Table 1.

Table 1: Input Configurations and External (Exogenous) Input Parameters

Input Configuration #	External Input Parameters
0 (NAR)	
1	Hour of Day (HOD), Direct Normal Irradiance (DNI), Diffused Horizontal Irradiance (DHI)
2	HOD, DNI, DHI, Azimuth Angle, Zenith Angle
3	HOD, DNI, DHI, Azi. Angle, Zen. Angle, Cloud Coverage (CC) %
4	HOD, DNI, DHI, Azi. Angle, Zen. Angle, CC %, Relative Humidity
5	HOD, DNI, DHI, Azi. Angle, Zen. Angle, CC %, Rel. Humidity, Temperature

In a majority of time series applications, there can tend to be a great variance in the transient periods of the data. This is why nonlinear approaches are recommended over linear approaches for time series problems. A nonlinear autoregressive neural network describes a discrete, non-linear, autoregressive model that can be expressed in the equation below [11] [27].

$$y(t) = f\big(y(t-1), \dots y(t-d)\big) \qquad \text{Equation 2}$$

Equation 2 represents how NAR methods are used to predict the future value of a data series *y* at the time *t* using the past values *d* of the time series. The function is unknown prior to training and optimal weights and neuron biases are determine within the training stage in order to approximate the function.

The network setup of the NAR method is displayed below in Figure 15. The network will be created and trained in open loop form. Training with open loop (single-step) prediction is more efficient than with closed loop (multi-step) prediction because it allows us to supply the network with correct feedback inputs even as we train it to produce the correct feedback outputs [27]. The NAR network is dependent on the number of feedback delays and the number of neurons in the

hidden layer within the network. Both of these values are adjustable and are effectively optimized by trial-and-error testing. Although, drastic increases of the number of neurons per hidden layer increases the complexity and decreasing this value can lower the computing power and generalization of the network.

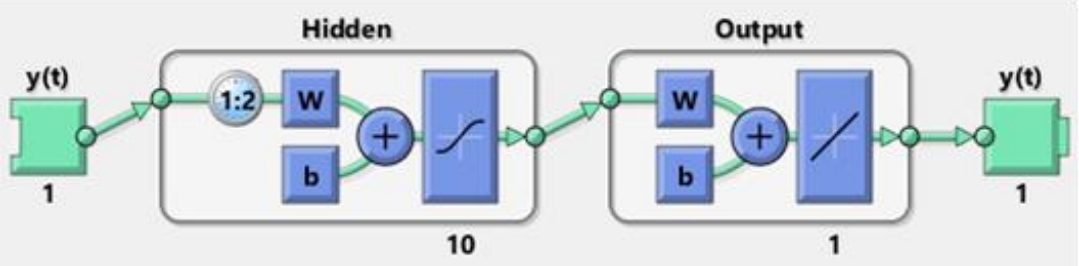

Figure 15: Neural Network Setup for an Open Nonlinear Autoregressive (NAR) Time Series Problem

To properly improve the results of the NAR network of the GHI data, it can be beneficial to include additional exogenous inputs. Nonlinear autoregressive with exogenous (external) inputs, NARX, allows these additional inputs to be implemented into the network evaluation. NARX methods, as seen below in Equation 3 predict the data series *y* at time *t* given past values *d* of series *y* and another external input series *x* at time *t*. The external inputs can be single or multidimensional.

$$y(t) = f\big(x(t-1), \dots, x(t-d), y(t-1), \dots y(t-d)\big) \qquad \text{Equation 3}$$

The NARX approach is a nonlinear model that approximates time step ahead values of a time series based on previous outputs and external data. The neural network setup of this approach can be seen below in Figure 16. Similar to the NAR model, the NARX approach is also

dependent on the amount of feedback delays and the number of neurons within the hidden layer. These values are also optimally determined by trail-and-error testing.

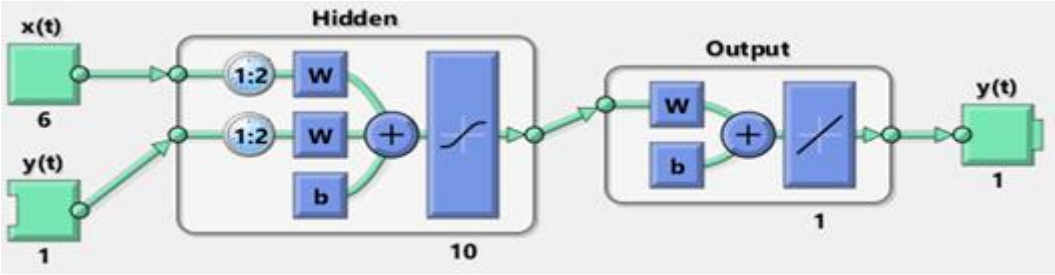

Figure 16: Neural Network Setup for an Open Nonlinear Autoregressive with External Input (NARX) Time Series Problem

The Levenberg-Marquardt (LM) algorithm was used as the learning algorithm and it was used for both network types and both data set locations. LM algorithm networks have been proven to be the optimum prediction model when compared to the other algorithms such as: Bayesian regularization (BR), the Scaled Conjugate Gradient algorithm, etc. [12] [28] [29]. Although this algorithm typically requires more memory, it often produces precise results in less computational time.

After determining the optimal model algorithm, the optimal number of delays and neurons were determined to further improve the predictive model. In order to do this number of neurons in the hidden layer were kept constant at 10 and trial-and-error testing was done using several delay variables. Following optimal delay determination, that value was kept constant to determine the appropriate number of neurons to produce the best ANN. The values were then used to evaluate the remote data set according to several time periods to determine how much historical irradiance and meteorological data is necessary to provide accurate data for the local data set. They

included seasonal (3 month), ½ year, 1 year, 2 year, and 3 year forecasting. The data ranged from January 1, 2014 to December 31, 2016.

Following the evaluation of the remote data set, the local data set was utilized within the ANN. The optimal model algorithm was used from the NAR and NARX input configuration testing for the remote data set. The optimal number of feedback delays and number of neurons within the hidden layer for the local irradiance set were determined using the exact procedure utilized for the remote data set.

Photovoltaic Modeling and Simulation

It is important that the model of the PV panel produces worthy results. The model was a complete mathematical representation of the PV system at hand. The system was modeled by implementing the governing equations in MATLAB Simulink. Simulink is graphical programming environment used for modeling, simulating and analyzing multi-domain dynamic systems. The primary interface is a graphical block diagramming tool with several customizable block libraries. It essentially allows you to model algorithms and physical systems using block diagrams. You can model both linear and nonlinear systems while incorporating real life factors, such as electrical circuits.

In the previous chapter, it was determined that a one-diode (five parameter) model is an appropriate representation of a PV module. For this project, a Renogy 100W Monocrystalline PV Module (RNG-100D) was used as the bases for the model. The equivalent electric circuit of the PV module can be seen in Figure 17: Equivalent Electric Circuit of a One-Diode (Five Parameter) PV Module. The model was then evaluated using the STC of 1 kW/m^2, a 1.5 air mass spectrum, and a cell temperature of 298.15 K (25℃).

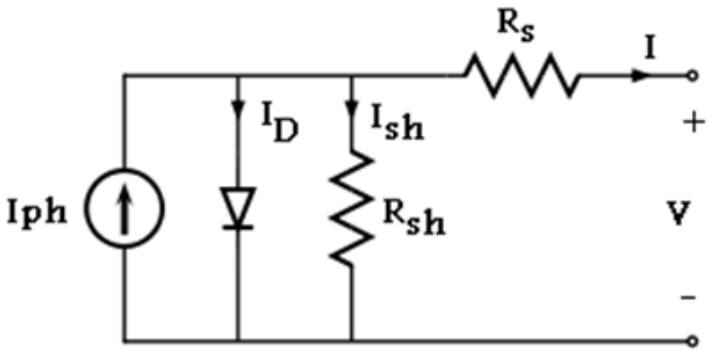

Figure 17: Equivalent Electric Circuit of a One-Diode (Five Parameter) PV Module

In order to duplicate this module it is then important to evaluate all of the governing equations and represent them within the MATLAB Simulink block program. The program gives the ability to mathematically solve the system's equations simultaneously.

With reference to the model in Figure 17, there are five unknowns to determine in order to characterize the system:I_{ph}, I_d, I_{sh}, R_{sh}, and R_s. These values are not usually expressed by PV manufactures, but the can be deduced mathematically [Eq. 2-9]. Equation 4 represents the module photocurrent as it is expressed solely from operational and STC values.

$$I_{ph} = G_r\left[I_{sc} + k_{l_{sc}}\left(T_{op} - T_{ref}\right)\right] \qquad \text{Equation 4}$$

In order to determine the diode current, seen in Equation 4, diode reversed saturation current at the cell operating temperature (Equation 5) and the diode reversed saturation current (Equation 6). The diode reversed saturation current at the cell operating temperature is next priority, because it can be determined by data sheet parameters and operational conditions as *k* (1.38e-23) and q (1.6e-19) are constants. Equation 5 constitutes to Equation 6 and ultimately Equation 4 correlates to the shunt resistance.

$$I_d = \left[e^{\frac{(V+IR_s)}{(nV_tCN_s)}} - 1\right] I_s N_p \quad \text{Equation 5}$$

$$I_{rs} = \frac{I_{sc}}{\left[e^{\left(\frac{V_{oc}q}{kCT_{op}n}\right)-1}\right]} \quad \text{Equation 6}$$

$$I_s = I_{rs}\left(\frac{T_{op}}{T_{rep}}\right)^3 e^{\left[\frac{qE_g}{nk}\left(\frac{1}{T_{op}}-\frac{1}{T_{ref}}\right)\right]} \quad \text{Equation 7}$$

The following equations are then solved in cohesion to ultimately determine the total current of the system.

$$V_t = \frac{kT_{op}}{q} \quad \text{Equation 8}$$

$$V_{oc} = V_t \ln\left(\frac{I_{ph}}{I_s}\right) \quad \text{Equation 9}$$

$$I_{sh} = \frac{V + IR_s}{R_{sh}} \quad \text{Equation 10}$$

$$I = I_{ph}N_p - I_d - I_{sh} \quad \text{Equation 11}$$

After determining the governing equations, it is important to be able to state all of the characteristics that are represented on the PV data sheet. These characteristics are represented in Table 2 as:

Table 2: RNG-100D PV Module Manufacturer Data Sheet Parameters

Parameters	Values
P_{mp}	100 W
I_{mp}	5.29 A
V_{mp}	18.9 V
V_{oc}	22.5 V
I_{sc}	5.75 A
$K_{V_{oc}}$	-0.30 %/℃
$K_{I_{sc}}$	0.04 %/℃
C	36 (4 x 9)

The parameters represented in Table 2 were determined under the STC and were implemented into the several unknown parameter equations expressed above. The model representation of the parameter inputs, Equation 5 though Equation 11, and the entire system can be seen below in Figure 18 through Figure 27.

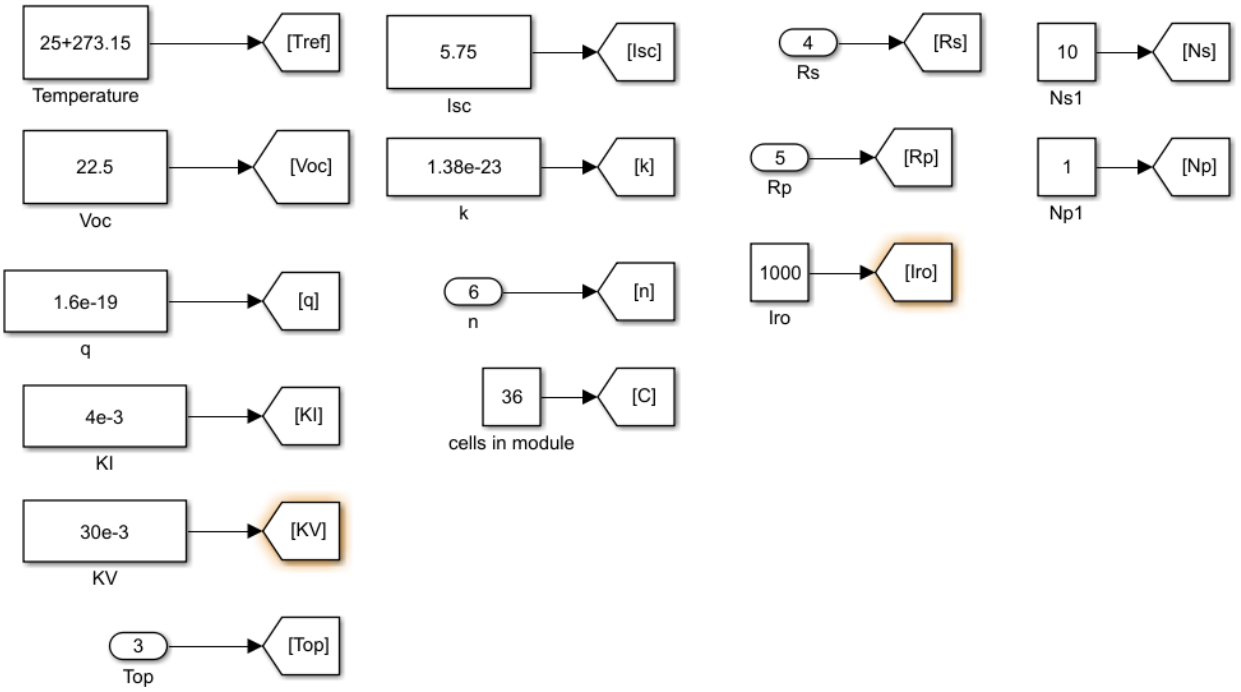

Figure 18: Input Parameters for the Simulation Model

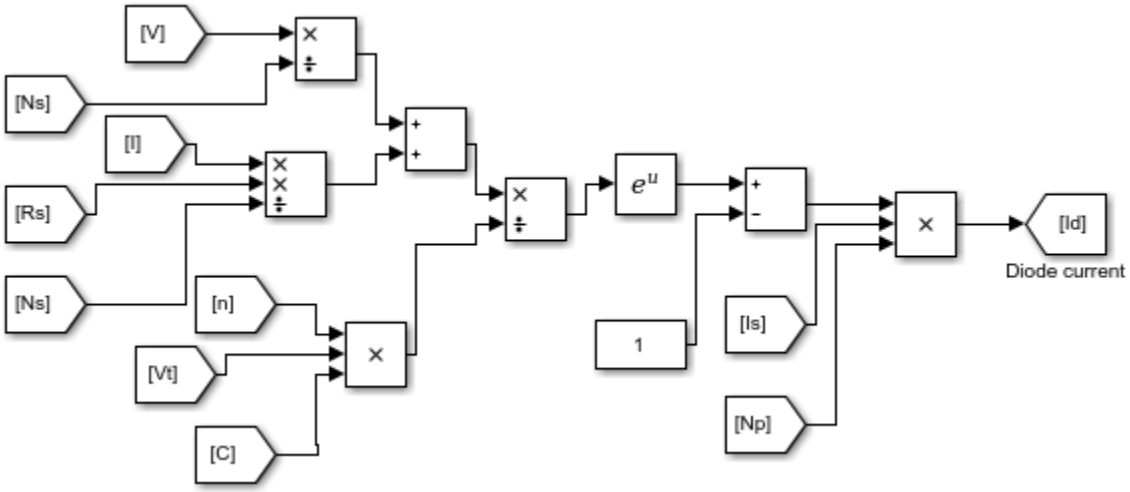

Figure 19: Modeled Circuit for Equation 5

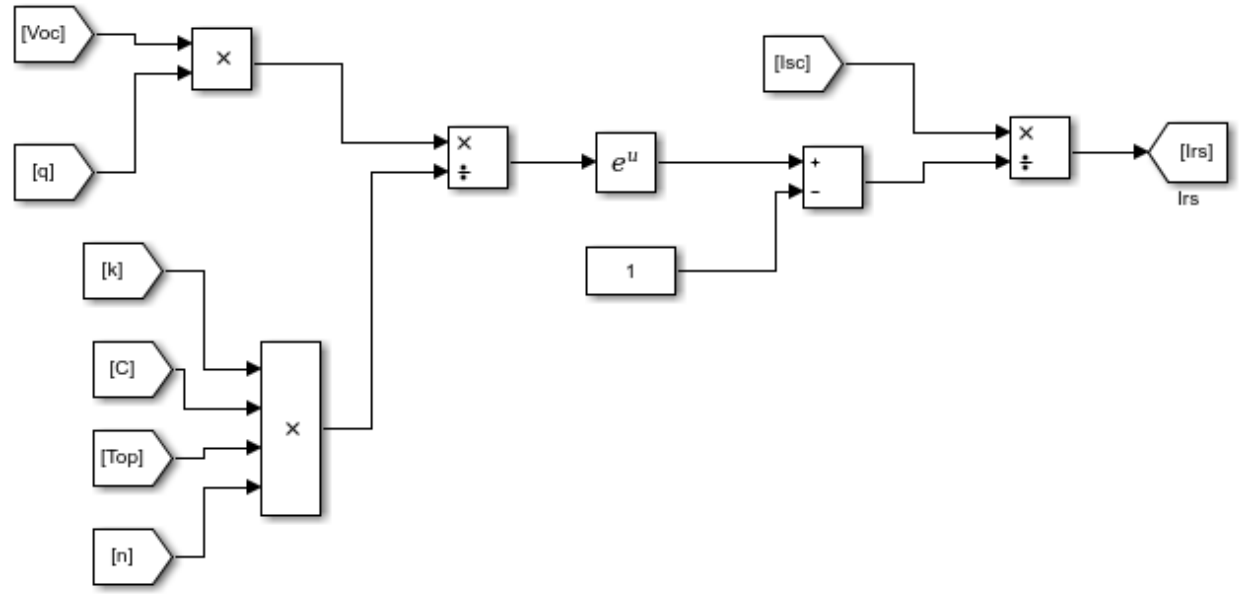

Figure 20: Modeled Circuit for Equation 6

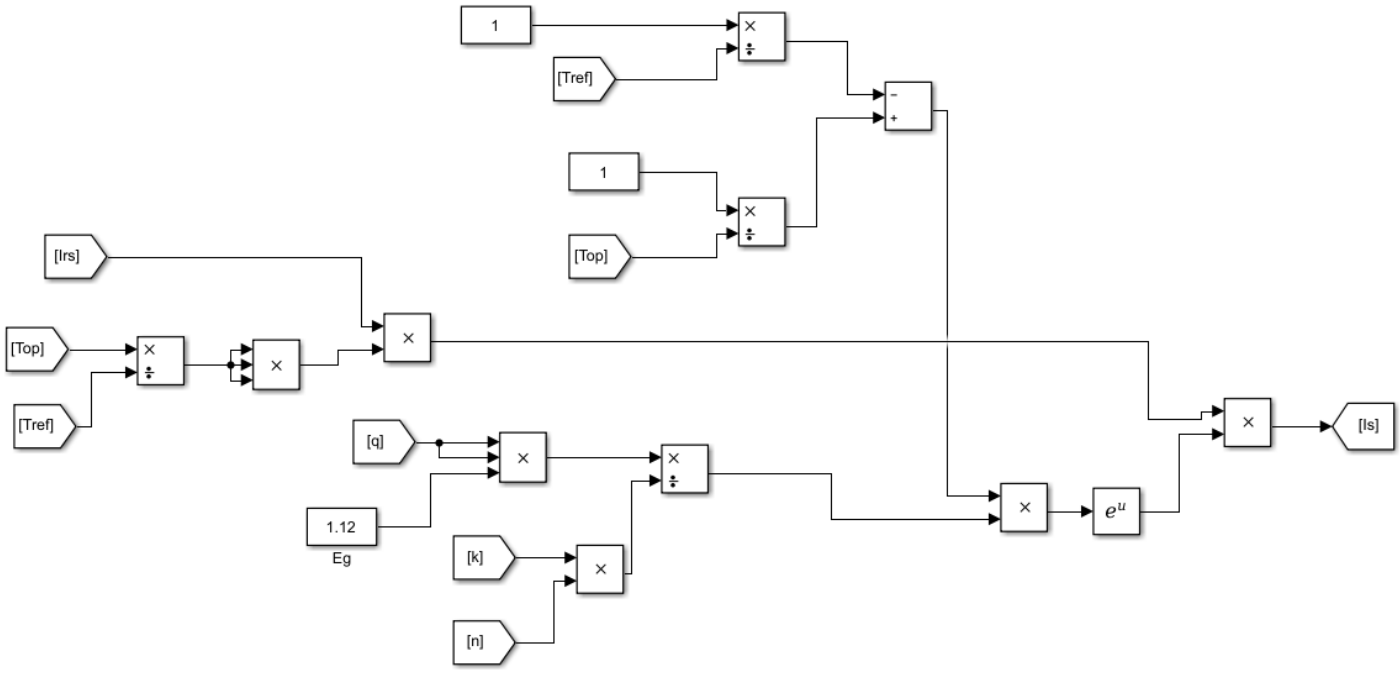

Figure 21: Modeled Circuit for Equation 7

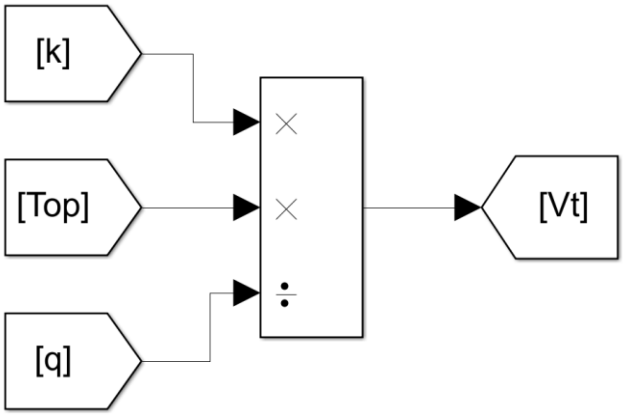

Figure 22: Modeled Circuit for Equation 8

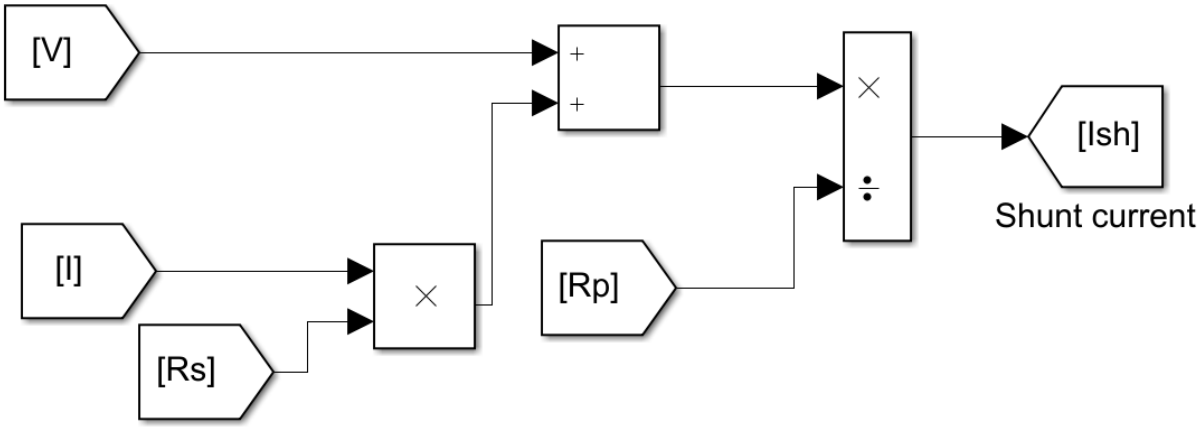

Figure 23: Modeled Circuit for Equation 10

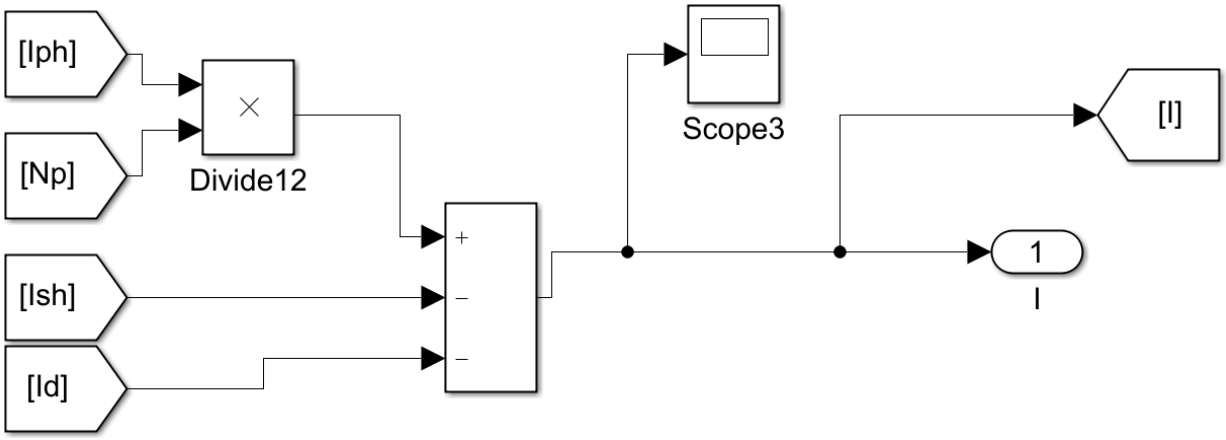

Figure 24: Modeled Circuit for Equation 11

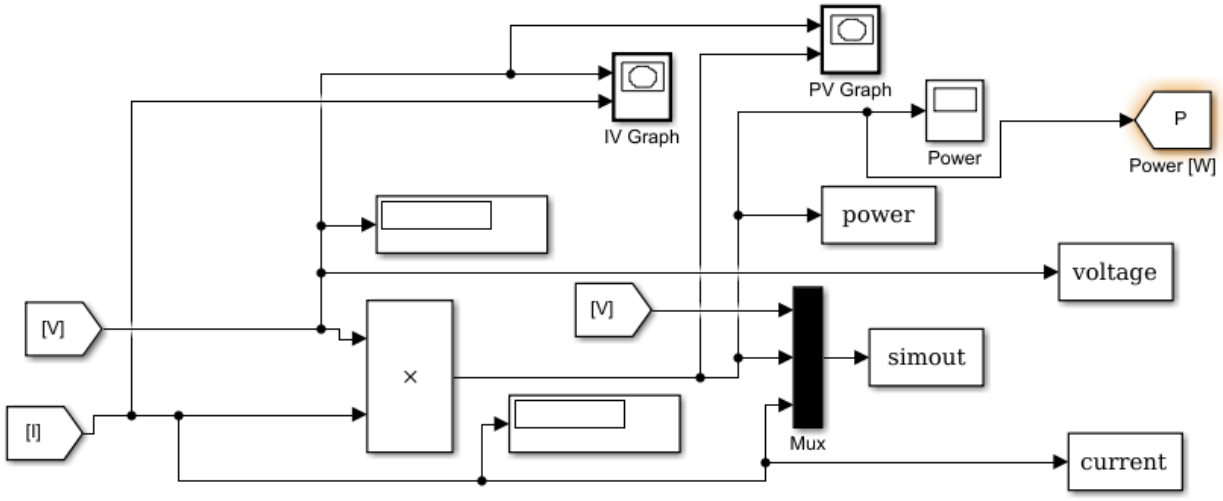

Figure 25: Output Circuit of the PV Model

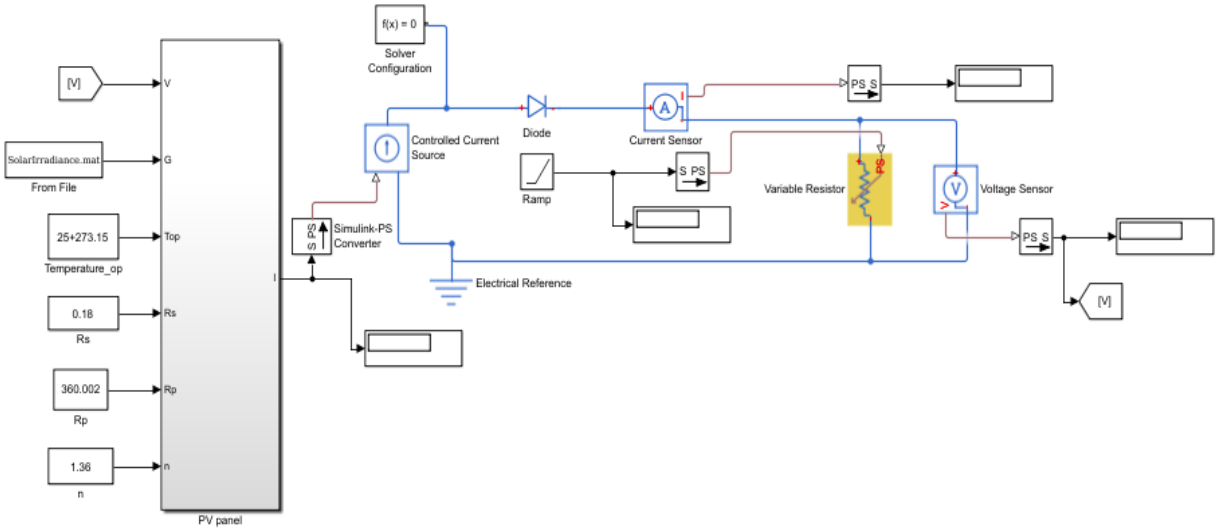

Figure 26: Presentation of Entire PV Model

As a result of the simulation, the total voltage and current was determined. Current versus voltage and power versus voltage curves were developed to display the overall operation of the system at STC. The results were then compared to the curves provided by the manufacture, and then the model was evaluated at varying temperatures and irradiances. Figure 27 is a graphical representation of the PV parameters displayed on the typical *I-V* and *P-V* characteristics curve.

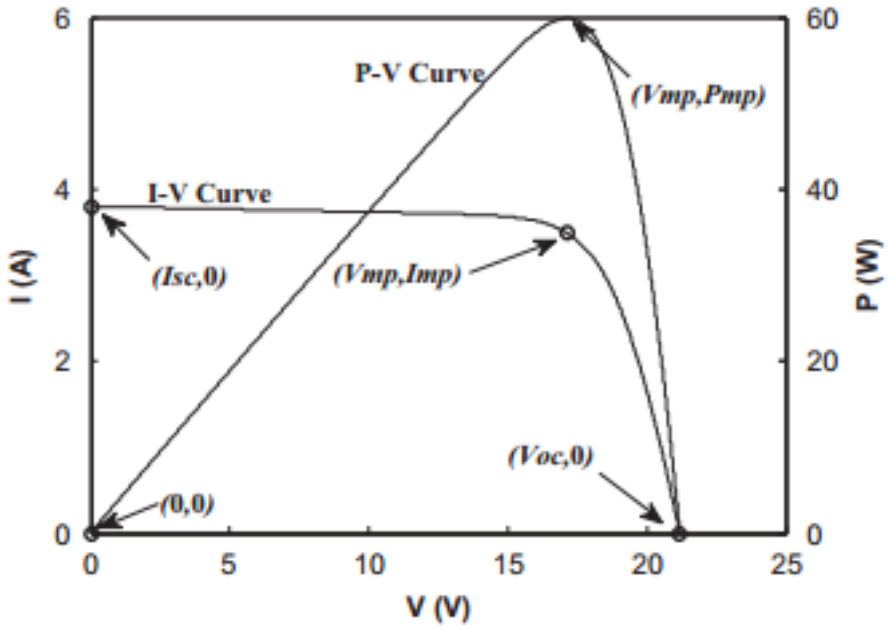

Figure 27: I-V and P-V Characteristics Curve

Domestic Electric Water Heater Modeling and PV Implementation

A typical DEWH works by including two heating elements at two different levels of the tank. Both of these elements are usually applied power from the grid, and they operate non-simultaneously. In order for the elements to operate in this manner, the two elements are thermostatically controlled and only operate when a desired temperature is reached in the area of the tank near that particular element. When that temperature is reached, the other element begins the heating process or both elements are either non-operational until hot water demand is necessary. Due to a process known as thermal stratification, the hot water will rise in the tank due to high temperature water having less density the colder water. This is why the hot water draw is usually pulled from the top of the tank and the cold water is supplied in the bottom. Thermal stratification is a desired phenomenon as it aids in raising the temperature of the water, but it complicates being able to model the system.

In order to simplify the model of the DEWH, it was assumed to be a one-node model that is fully mixed. This negated the need to model the tank as two different layers and developing a second-order differential equation known as a one-node model. This model is valid when the DEWH's tank is empty of hot water or full of hot water [23]. The thermal water heater system diagram of the system is shown below in Figure 28.

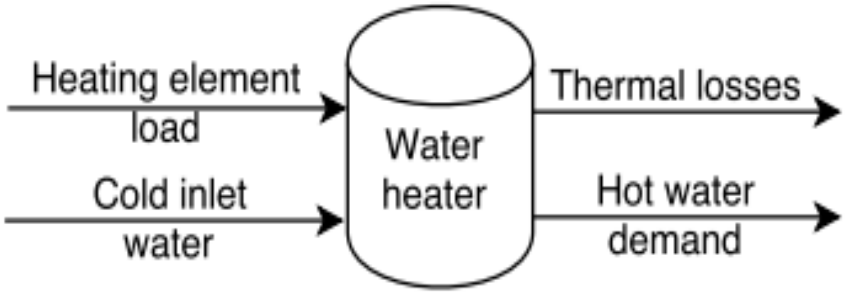

Figure 28: Thermal Water Heater System Diagram

By manipulating the thermal heat transfer equations, the mathematical representation of the system can be seen in Equation 12.

$$Q_{ele} - \dot{m}C_p(T_w - T_{imlet}) + UA_{wh}(T_a - T_w) = C_w \frac{dT_w}{dt} \qquad \text{Equation 12}$$

The tank model was created using MATLAB Simulink. The tank was model as a 4500 watt, 40 gallons, and operated based on the hourly average hot water profile, as provided by NREL Buildings Research [30]. The inlet and ambient temperature of the water were both assumed to 292.15 K, and the coefficient terms of both water and the tank were found accordingly. A relay was added to the tank model to serve as the typical thermostatic control used by DEWHs. The block diagram of the model can be seen in Figure 29 below.

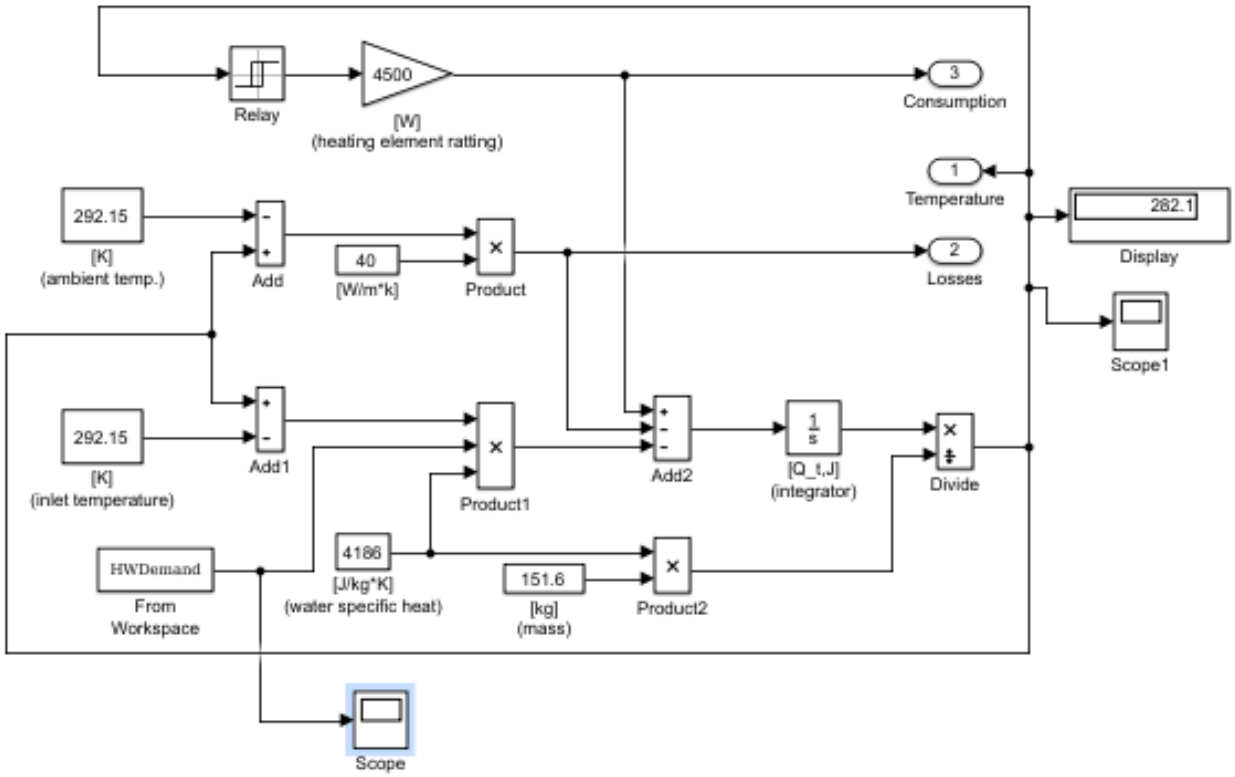

Figure 29: Domestic Electric Water Heater Simulink Block Diagram Model

CHAPTER 4: RESULTS AND DISCUSSION

Solar Irradiation Data Collection Results

Concluding the installation and configuration of the solar tracker and its equipment, the information received from the data logger was applied to a specified URL (http://141.165.72.78/). The temperature, direct normal irradiance (DNI), global horizontal irradiance (GHI), diffused horizontal irradiance (DHI), and far infrared radiation is continuously displayed by a minute average and hourly average. These results were displayed and observed, because they are most likely to affect the potential of PV energy. It is also displayed in the data spread that the configuration determined the standard deviation of the resulting temperatures and irradiances. The standard deviation presents the differences of the results over the span of the minute and hour.

Figure 30 is a 24-Hour graphical representation of the average minute direct normal irradiance, average global irradiance, average diffused irradiance, and the average far infrared radiation in the span of a day (September 17, 2017). On this particular day, the solar tracker represented a typical display of the solar irradiance within southeastern region of Georgia. The DNI irradiance was at its peak value around 2:00 pm to 4:00 pm and this is typical as the sun is near its highest point in the sky. The global irradiance resembles the results of the DNI and the value decreases as the cloud coverage increased. The diffused irradiance was shown as the lowest value in Figure 30, especially on a day where sunlight is abundant, because it is a representation of the amount of irradiance surrounding the area; excluding DNI. The global irradiance is a combination of both DNI and diffused irradiance and its value typically falls between the two. On days with minimal overcast, the irradiance data was consistently presented in a bell-like curve and

completely nonexistent through sundown. Far infrared radiation is shown to be constant around $300\frac{W}{m^2}$.

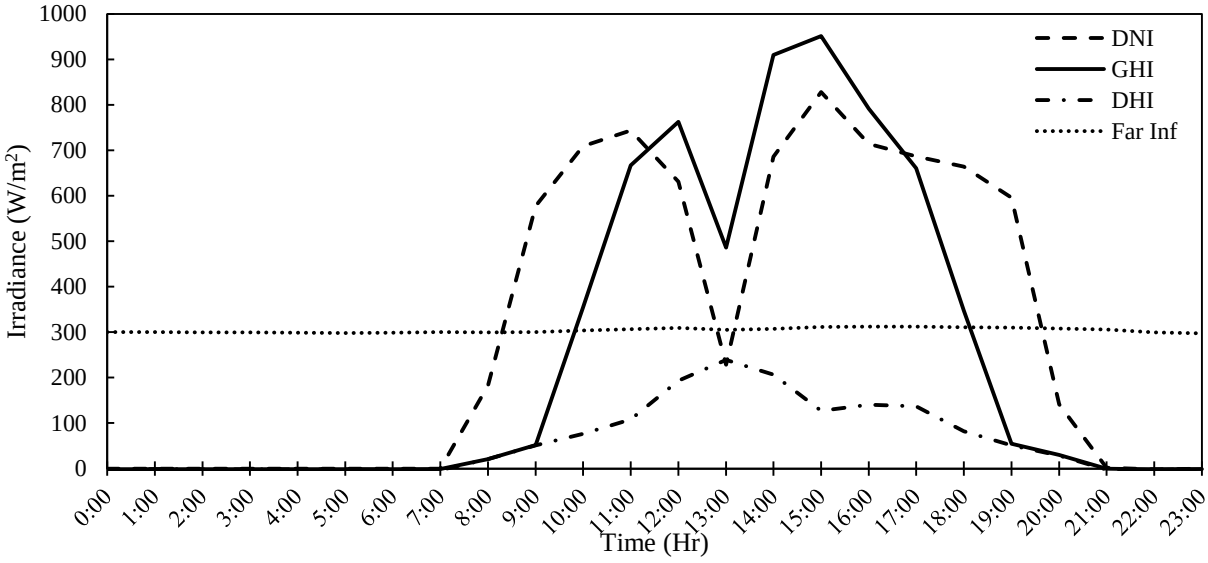

Figure 30: Solar Irradiance Data over a 24 Hour Period (September 17, 2017)

Remote Solar Irradiation Data Forecasting Results

This section highlights all the tests that were utilized and the experimental settings for the prediction of solar irradiance at the NREL Golden, Colorado location. As previously stated, it was important to determine the ANN problem needed to produce optimal results. Different input configurations were examined and comparisons were drawn between the results of the NAR and NARX models. The training method, delay parameters (2), and number of neurons within the hidden layer (10) were all kept constant.

Table 3 and Figure 31 shows the average mean squared error (MSE) of five trials for all six input configurations. Input configuration #0 is considered to be the NAR solution, as it uses no external inputs to predict future global horizontal irradiance data. Inputs 1 through 5 all have varying external inputs (Table 1) to see which affect NARX models have on predicting GHI

data. The NAR model was produced the worst MSE and the NARX (input configuration #3) model produced to best MSE.

Table 3: MSE of the Input Configurations (Colorado Data Set)

Input MSE Comparisons (Levenberg-Marquardt)						
	Input Configuration #					
	(NAR) 0	**1**	**2**	**3**	**4**	**5**
Trial 1	6.81E-03	4.35E-03	4.10E-03	4.00E-03	3.96E-03	5.66E-03
Trial 2	6.86E-03	4.70E-03	4.80E-03	3.30E-03	3.49E-03	4.69E-03
Trial 3	7.50E-03	4.96E-03	4.12E-03	4.34E-03	4.93E-03	4.97E-03
Trial 4	6.35E-03	5.01E-03	4.08E-03	4.25E-03	3.66E-03	4.55E-03
Trail 5	7.10E-03	4.37E-03	4.37E-03	4.65E-03	4.92E-03	5.14E-03
Avg.	**6.92E-03**	**4.68E-03**	**4.29E-03**	**4.11E-03**	**4.19E-03**	**5.00E-03**

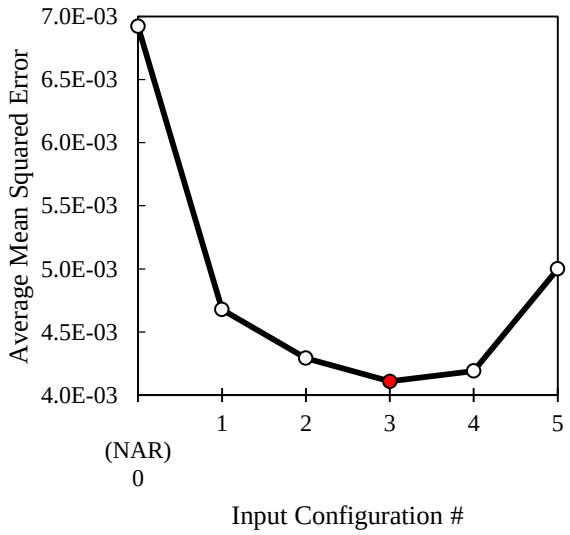

Figure 31: MSE of the Input Configurations Graph

Comparisons between the target and single-step ahead predicted data over a span of a year (October 1, 2016 to September 31, 2017) for the NAR and optimal NARX configurations can be seen in Figure 32 and Figure 33. Figure 34 and Figure 35 represents the same two graphs reduced to one month (October 1, 2016 to October 31, 2016) in order to better observe the results of the two ANN models.

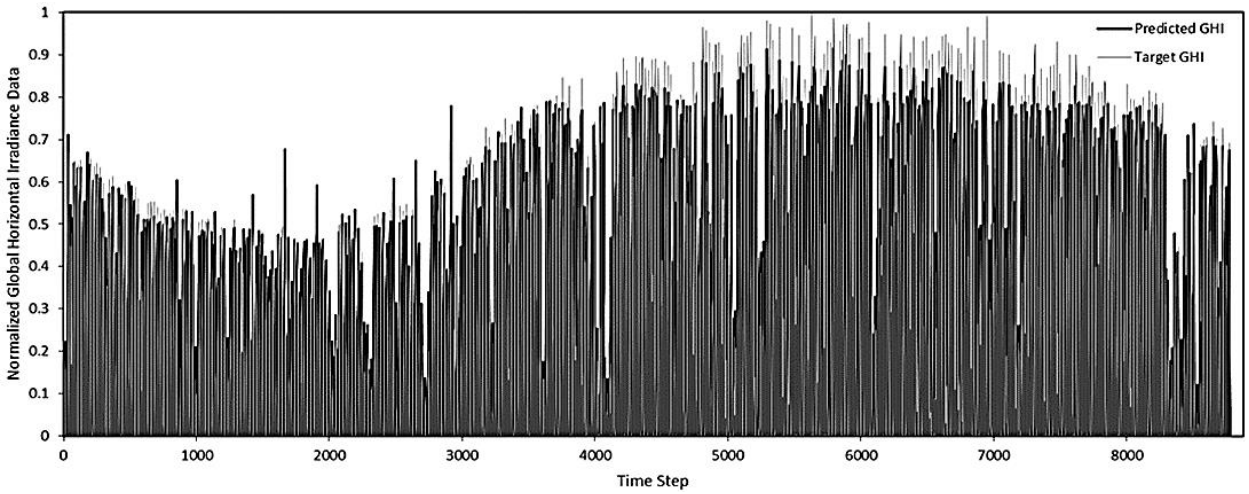

Figure 32: NAR Single-Step Ahead Prediction Comparison of Target Values vs. Predicted (October 1, 2016 – September 31, 2017)

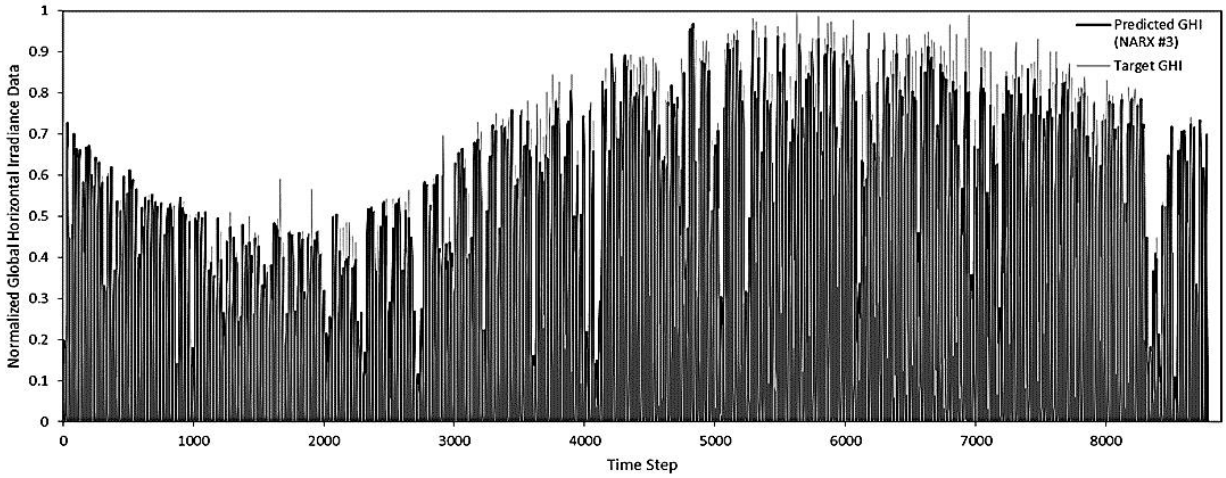

Figure 33: NARX Single-Step Ahead Prediction Comparison of Target Values vs. Predicted (October 1, 2016 – September 31, 2017)

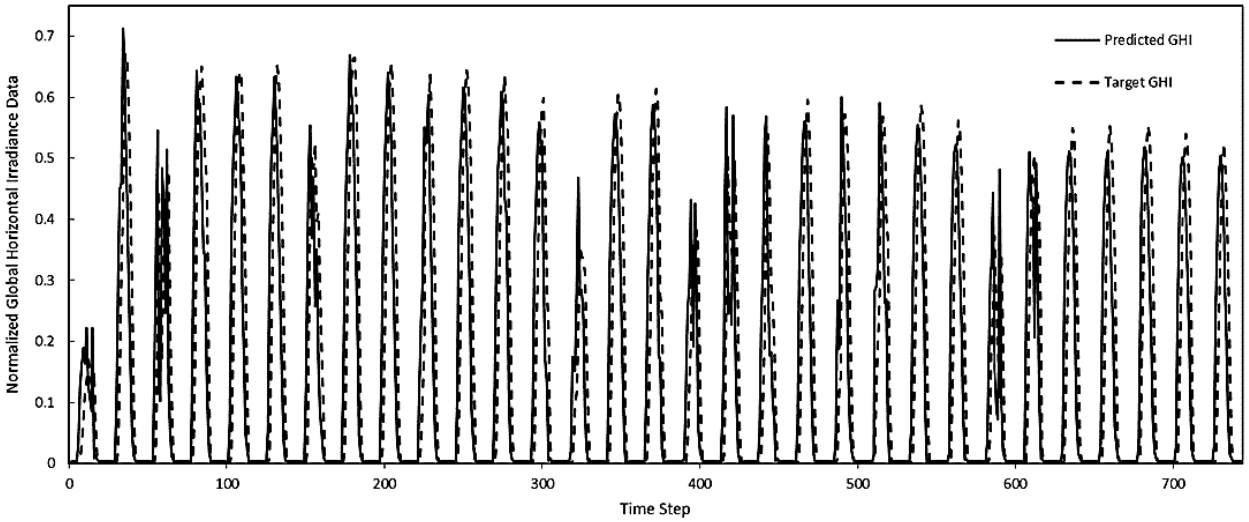

Figure 34: NAR Single-Step Ahead Prediction Comparison of Target Values vs. Predicted (October 1, 2016 – October 31, 2016)

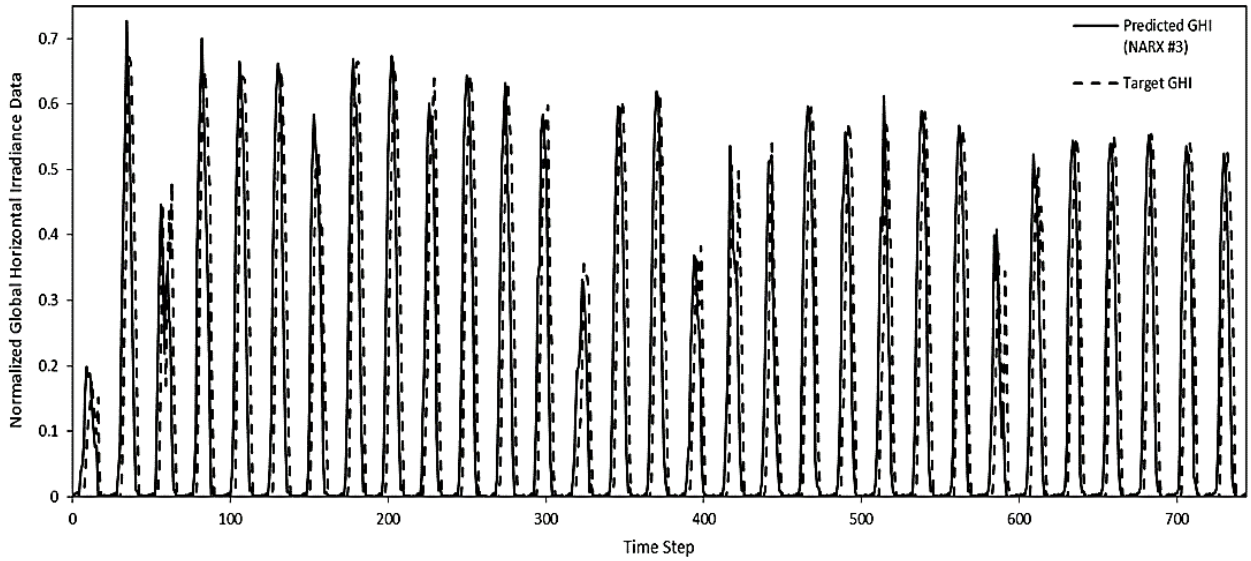

Figure 35: NARX Single-Step Ahead Prediction Comparison of Target Values vs. Predicted (October 1, 2016 – October 31, 2016)

The NARX input configuration #3 was used as the optimal model to determine the optimal amount of feedback delays and number of neurons within the hidden layer. The optimal delay parameter was determined by keeping number of neurons at the default value of 10. The delay parameters represent the number of hours the ANN utilized to execute the prediction. Eighteen different delay values were utilized to determine the optimal delay parameter. The delay values included were hourly values of d = 1, 2, 3, 4, 6, 8, 12, 14, 16, 18, and 20. In addition, to account for one or more days, the following delay values were included: d = 24, 36, 48, 60, and 72. With a fixed number of neuron parameter, trial and error testing was done in order to optimize the results.

Table 4 shows the average mean squared error (MSE) of five trials for each delay of the optimal NARX model. The minimal amount of delays to produce the lowest MSE was 2 hours with the results of 3 and 4 hours being closely related. The MSE continued to increase along with the delay values, so solar irradiance data is more accurately predicted with a lower amount of feedback delays.

After the determination of the optimal amount of delays, that value was used to determine the optimal number of neurons.

Table 5 depicts the MSE for the different number of neurons utilized from a range of one to fourteen. The value was increased until it was evident that the MSE was not improving, as

drastic increases in the parameter will result an increase in local maximum and cause overtraining during the LM learning algorithm. From the table, it can be deduced that the optimal MSE values occur at either four to five neurons in the hidden layer. Therefore, the optimal ANN consists of two delays and four neurons within the hidden layer.

Table 4: MSE of the Delay Parameter Obtained with the Optimal NARX Model Graph

	NARX Delays								
	1	2	3	4	6	8	10	12	14
Trial 1	4.84E-03	4.00E-03	4.44E-03	4.43E-03	3.92E-03	4.78E-03	4.78E-03	4.63E-03	5.27E-03
Trial 2	4.36E-03	3.30E-03	3.94E-03	4.56E-03	5.23E-03	4.40E-03	4.10E-03	4.79E-03	4.96E-03
Trial 3	4.04E-03	4.34E-03	3.78E-03	3.63E-03	5.09E-03	4.29E-03	4.78E-03	5.15E-03	4.97E-03
Trail 4	4.55E-03	4.25E-03	4.13E-03	4.60E-03	5.45E-03	4.90E-03	4.44E-03	3.79E-03	4.66E-03
Trail 5	4.69E-03	4.65E-03	4.29E-03	3.67E-03	4.09E-03	5.49E-03	5.95E-03	4.93E-03	3.86E-03
Avg.	4.49E-03	4.11E-03	4.12E-03	4.18E-03	4.76E-03	4.77E-03	4.81E-03	4.66E-03	4.74E-03
	16	18	20	24	28	36	48	60	72
Trial 1	4.60E-03	4.56E-03	4.98E-03	4.44E-03	5.48E-03	5.85E-03	5.52E-03	4.80E-03	6.56E-03
Trial 2	4.64E-03	5.35E-03	5.03E-03	4.34E-03	6.26E-03	5.86E-03	5.78E-03	4.68E-03	7.28E-03
Trial 3	4.10E-03	4.95E-03	4.24E-03	4.00E-03	5.55E-03	4.00E-03	4.81E-03	5.90E-03	5.96E-03
Trail 4	4.69E-03	5.03E-03	4.42E-03	5.24E-03	5.80E-03	5.72E-03	5.84E-03	7.50E-03	5.79E-03
Trail 5	4.46E-03	4.29E-03	4.46E-03	5.49E-03	5.71E-03	5.10E-03	6.19E-03	4.85E-03	8.49E-03
Avg.	4.50E-03	4.83E-03	4.63E-03	4.70E-03	5.76E-03	5.31E-03	5.63E-03	5.55E-03	6.81E-03

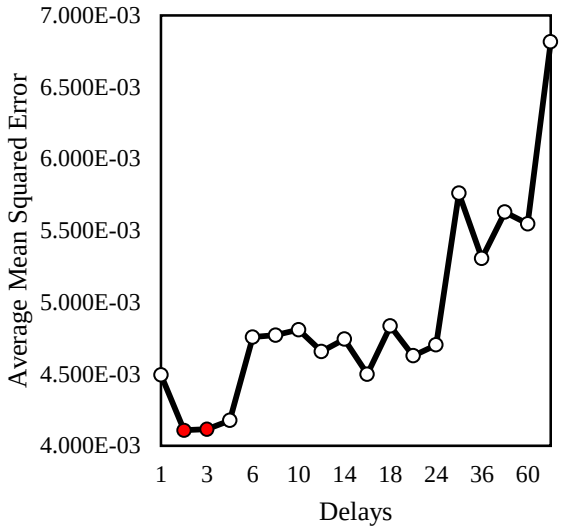

Figure 36: MSE of the Delay Parameter Obtained with the Optimal NARX Model Graph

Table 5: MSE of the Number of Neurons within the Hidden Layer Parameter Obtained with the Optimal NARX Model

	NARX - Number of Neurons within Hidden Layer								
	1	2	3	4	5	6	8	10	12
Trial 1	5.44E-03	3.91E-03	5.11E-03	3.74E-03	4.24E-03	4.80E-03	4.14E-03	4.60E-03	4.15E-03
Trial 2	6.44E-03	5.13E-03	4.67E-03	4.42E-03	4.14E-03	3.98E-03	4.11E-03	4.80E-03	5.05E-03
Trial 3	6.26E-03	5.33E-03	3.98E-03	4.53E-03	4.58E-03	4.75E-03	5.22E-03	4.12E-03	4.31E-03
Trail 4	5.83E-03	4.19E-03	3.47E-03	3.84E-03	4.05E-03	4.36E-03	4.21E-03	4.68E-03	4.92E-03
Trail 5	6.85E-03	4.71E-03	4.26E-03	4.46E-03	4.06E-03	4.10E-03	5.04E-03	4.57E-03	4.54E-03
Avg.	6.16E-03	4.65E-03	4.30E-03	4.20E-03	4.21E-03	4.40E-03	4.54E-03	4.55E-03	4.60E-03

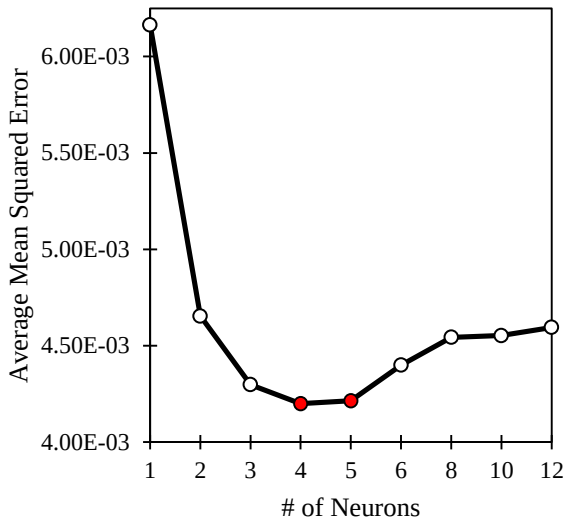

Figure 37: MSE of the Number of Neurons within the Hidden Layer Parameter Obtained with the Optimal NARX Graph

After the experimentation was completed, time dependent solar irradiance forecasting was conducted to determine the appropriate amount of time necessary to accurately predict values. It was also done to determine the best times to predict. The optimal model that was determined above was used for all of these ANNs. The time dependent problems were dependent on seasonal (3 month), ½ year, 1 year, 2 year, and 3 year solar forecasting.

Table 6 shows the MSE of the seasonal solar irradiance forecasting ANN. Each season was assessed for five trails and the average MSE was determined. Observing the results, the MSE is comparable for the fall and winter seasons and they are significantly lower than from the spring and summer seasons. Figure 39 through Figure 42 shows examples of the validation performance and the overall regression for each season. Figure 39 represents the validation performance of 0.0016277 and a regression value of 0.97955 for the winter season. Figure 40 represents the validation performance of 0.0058687 and a regression value of 0.96838 for the spring season. Figure 41 shows the validation performance of 0.0076095 and a regression value of 0.95938 for

the summer season. Figure 42 shows the validation performance of 0.0011962 and a regression value of 0.98455 for the fall season. Figure 43 through Figure 46 below displays plots of the normalized target values compared with the predicted values corresponding to the winter, spring, summer, and fall season respectively.

Table 6: MSE of the Optimal Setup for Seasonal Solar Irradiance Forecasting

3 Month (Seasonal) Solar Irradiance Forecasting MSE				
	Winter (12/21/2015 - 3/18/2016)	Spring (3/19/2016 - 6/19/2016)	Summer (6/21/2016 - 9/21/2016)	Fall (9/22/2016 - 12/20/2016)
Trial 1	2.79E-03	6.71E-03	8.14E-03	1.92E-03
Trial 2	1.06E-03	5.52E-03	6.64E-03	1.73E-03
Trial 3	1.52E-03	7.40E-03	5.54E-03	2.24E-03
Trail 4	1.84E-03	6.58E-03	6.99E-03	1.26E-03
Trail 5	1.53E-03	5.87E-03	6.27E-03	1.73E-03
Avg.	1.75E-03	6.42E-03	6.71E-03	1.78E-03

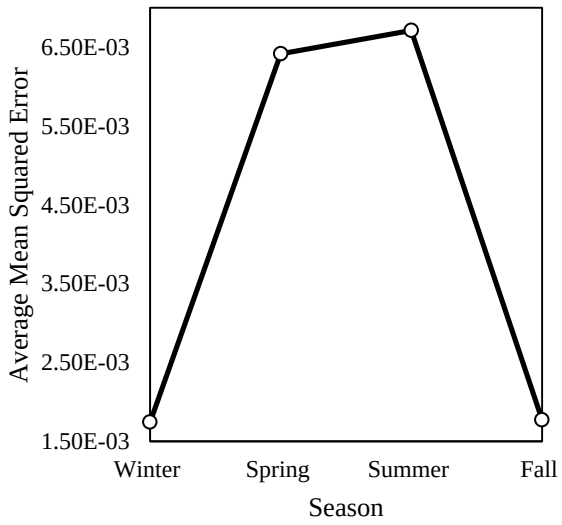

Figure 38: MSE of the Optimal Setup for Seasonal Solar Irradiance Forecasting Graph

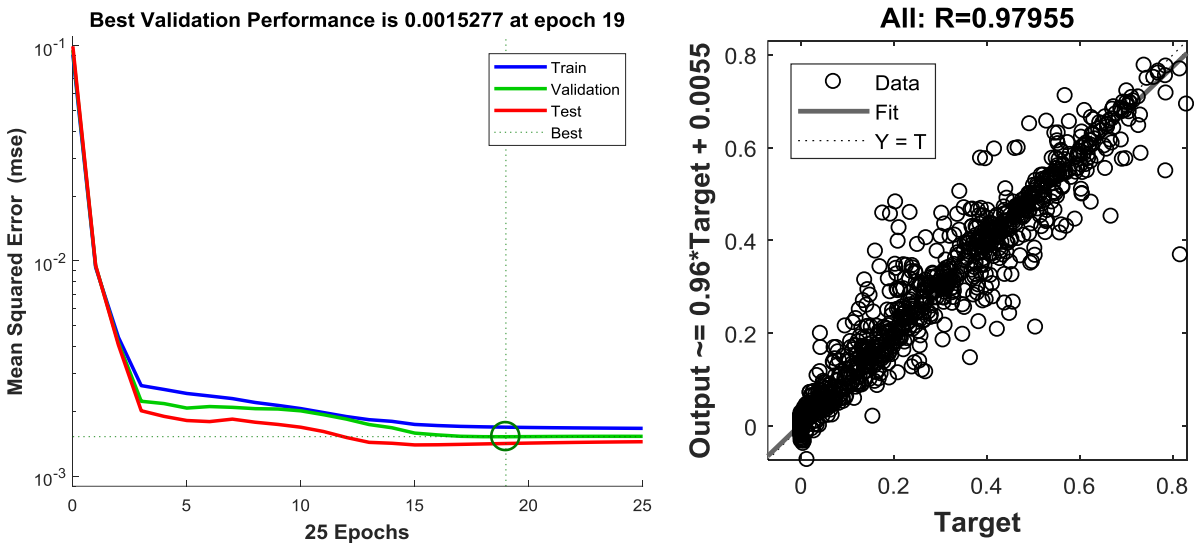

Figure 39: Winter Validation Performance and Regression Values of the MSE for the Normalized Data of Colorado using the NARX Model

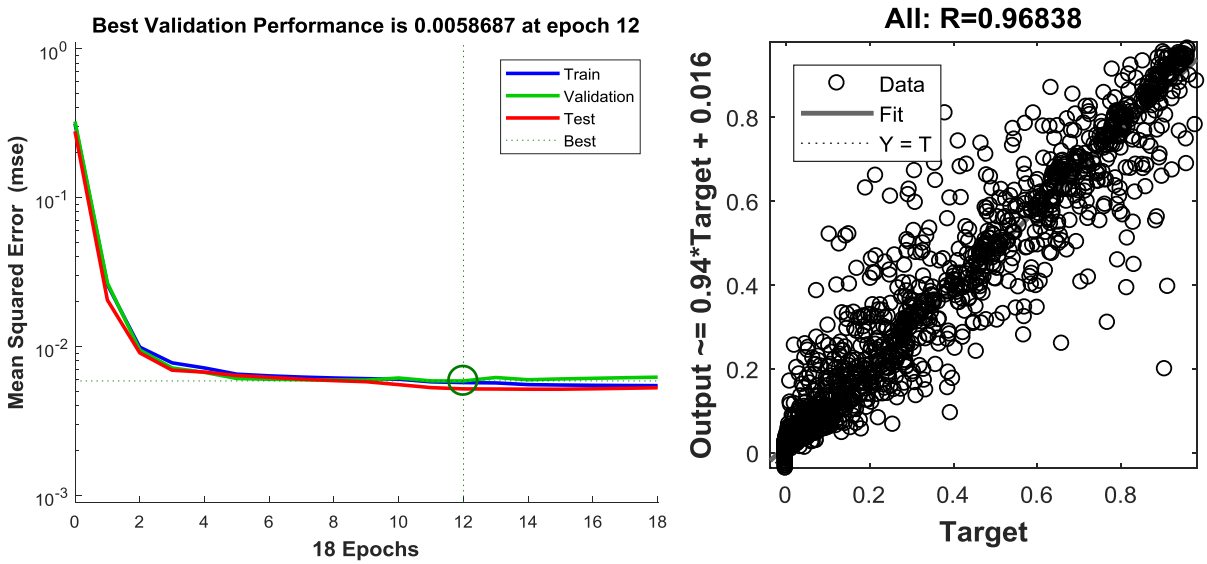

Figure 40: Spring Validation Performance and Regression Values of the MSE for the Normalized Data of Colorado using the NARX Model

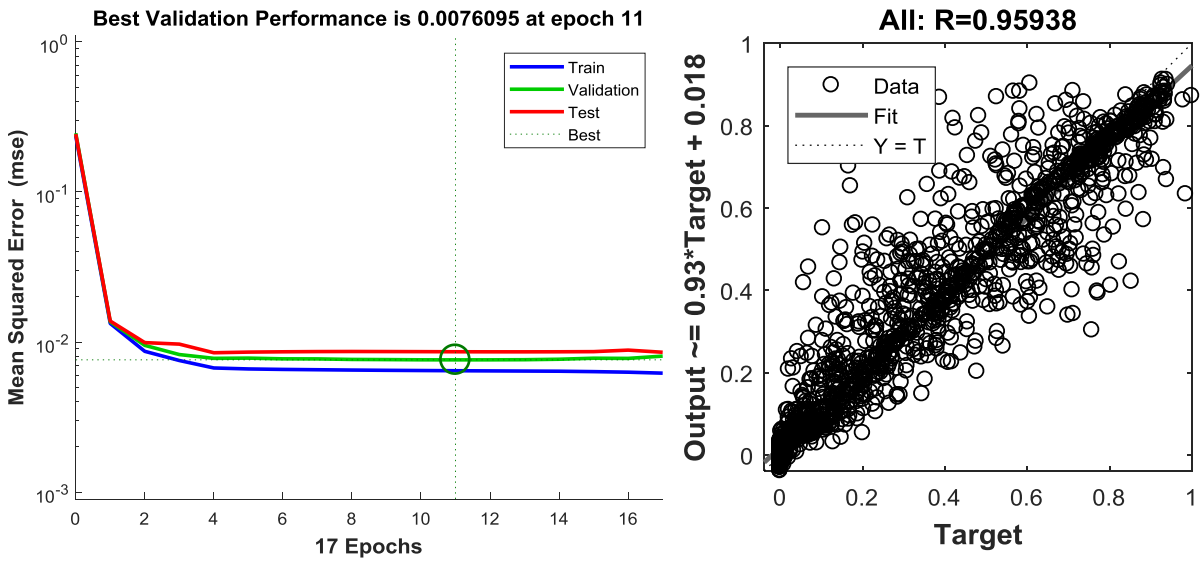

Figure 41: Summer Validation Performance and Regression Values of the MSE for the Normalized Data of Colorado using the NARX Model

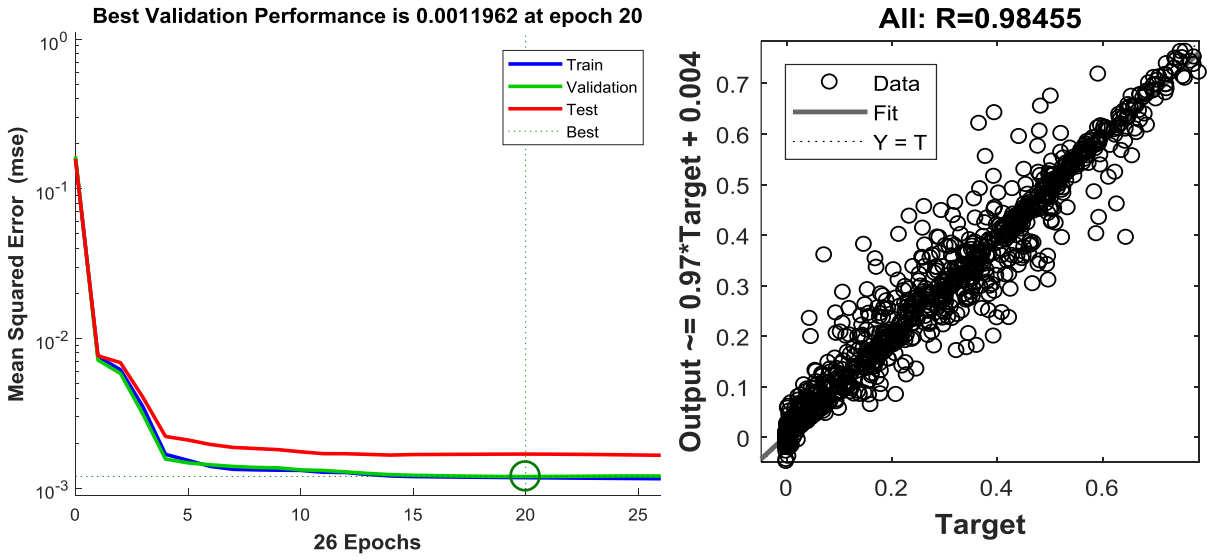

Figure 42: Fall Validation Performance and Regression Values of the MSE for the Normalized Data of Colorado using the NARX Model

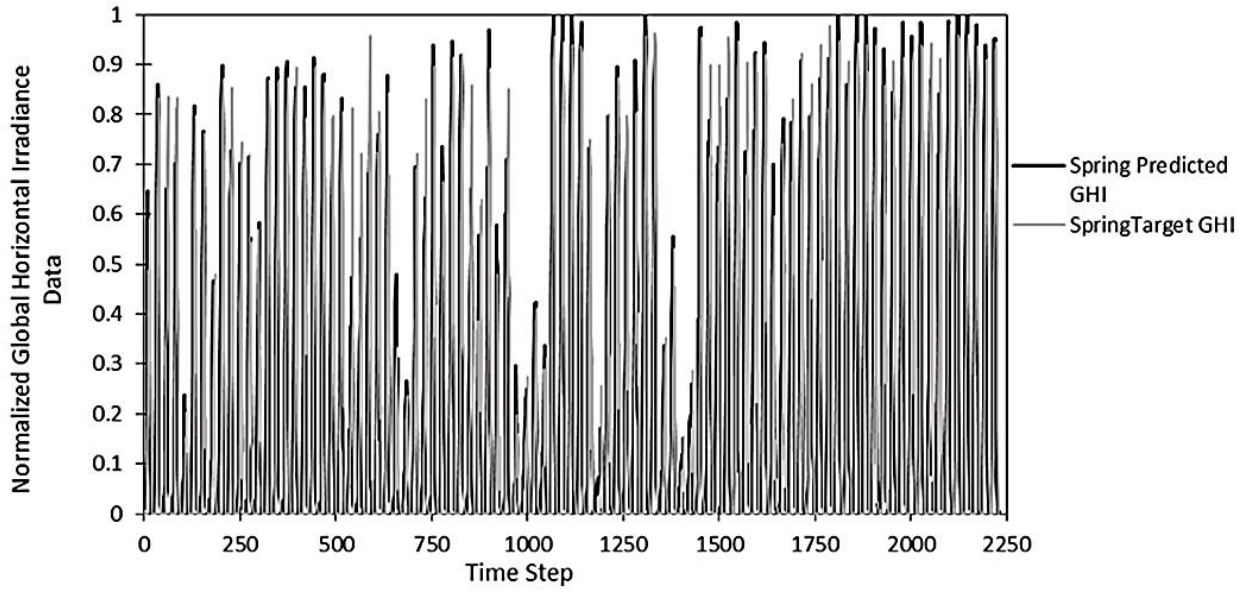

Figure 43: Spring Global Horizontal Irradiance Single-Step Ahead Prediction Comparison of Target Values vs. Predicted

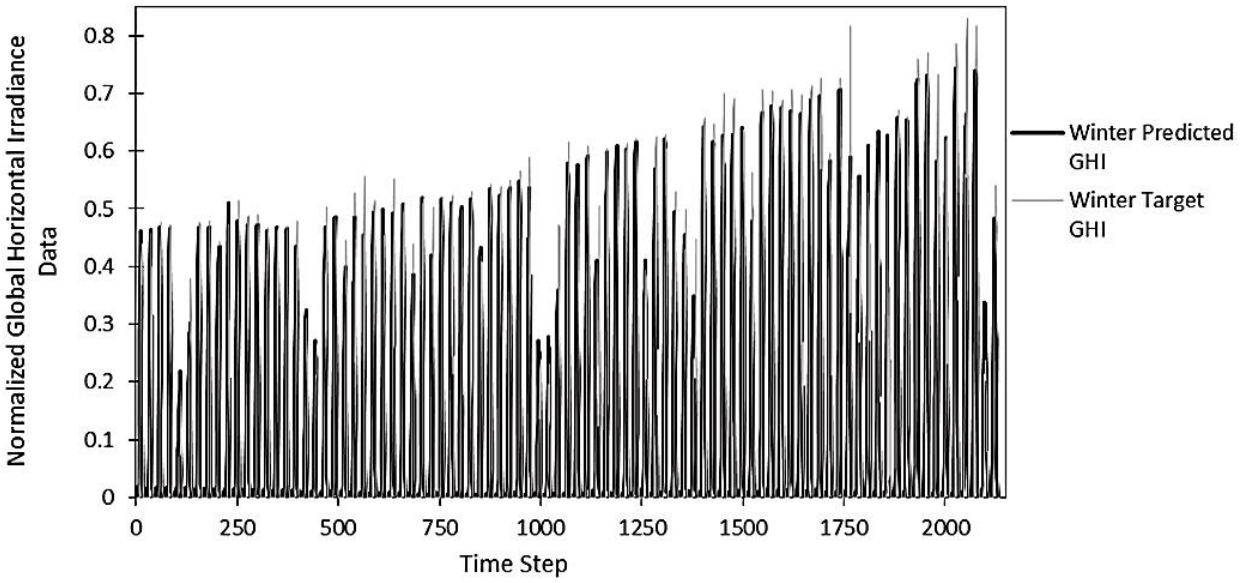

Figure 44: Winter Global Horizontal Irradiance Single-Step Ahead Prediction Comparison of Target Values vs. Predicted

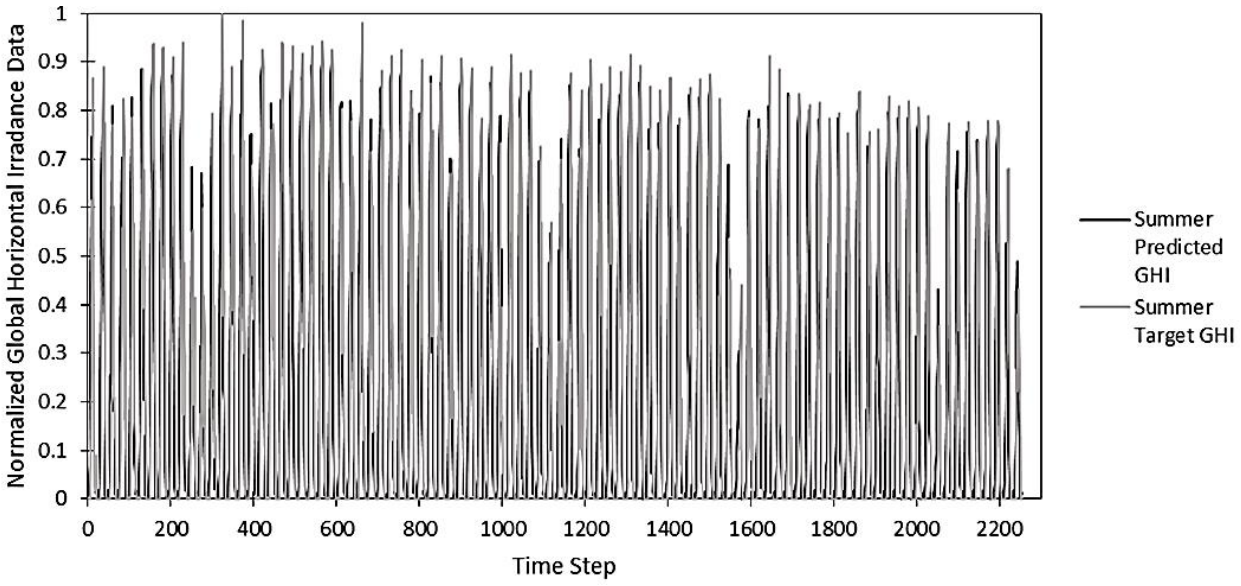

Figure 45: Summer Global Horizontal Irradiance Single-Step Ahead Prediction Comparison of Target Values vs. Predicted

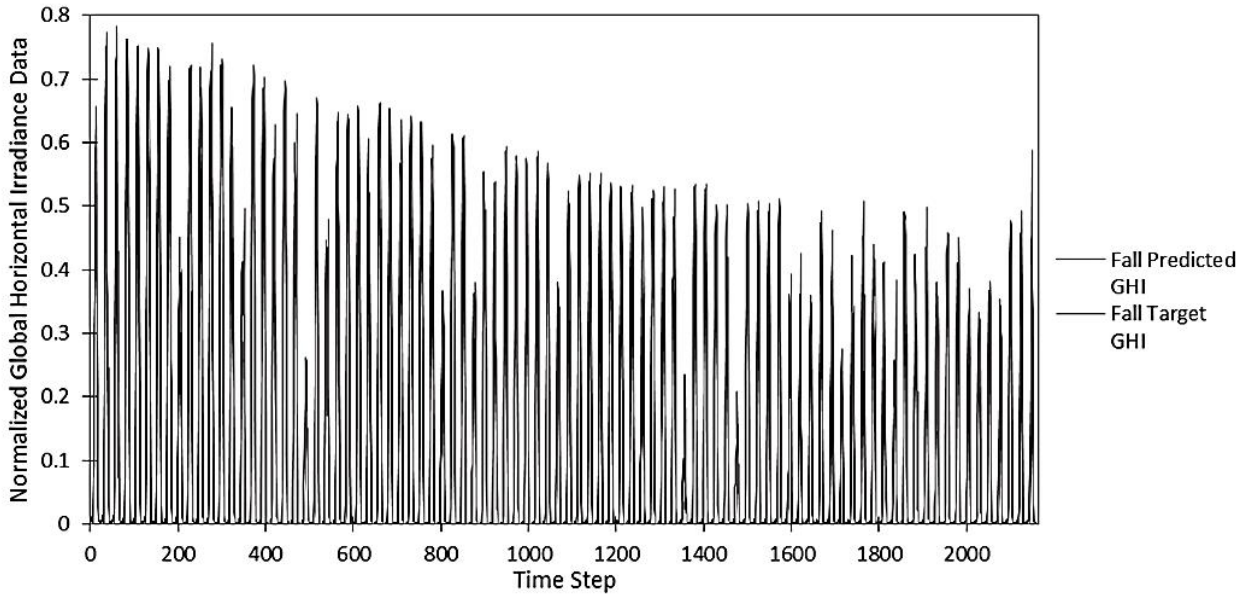

Figure 46: Fall Global Horizontal Irradiance Single-Step Ahead Prediction Comparison of Target Values vs. Predicted

Table 7 shows the MSE of the yearly solar irradiance forecasting ANN. Each data set was assessed for five trails and the average MSE was determined. As far as the ½ year data, the average MSE results are comparable for the 1st and 2nd six months at 4.22E-03 and 4.28E-03 respectively. The 1 year, 2 year, and 3 year data sets resulted in an average MSE of 4.66E-03, 4.32E-03, and 4.17E-03 respectively. Figure 48 through Figure 60 below shows examples of the validation performance and the overall regression for the yearly data sets. Figure 48 represents a performance of 0.0042167 and a regression value of 0.96928 for the 1st six month data set. Figure 49 represents a validation performance of 0.0040411 and a regression value of 0.96938 for the 2nd six month data set. Figure 50 shows a validation performance of 0.0048901 and a regression value of 0.96694 for the 1 year data set. Figure 51 shows a validation performance of 0.0044969 and a regression value of 0.9676 for the 2 year data set. Figure 52 shows validation performance of 0.0042406 and a regression value of 0.96462 for the three year data set. Figure 53 through Figure 57 below displays plots of the normalized target values compared with the predicted values corresponding to the yearly global horizontal irradiance forecasting.

Table 7: MSE of the Optimal Setup for Yearly Solar Irradiance Forecasting

Yearly Solar Irradiance Forecasting MSE					
	1/2 Year		1 Year	2 Years	3 Years
	1st 6 Months	2nd 6 Months			
Trial 1	4.64E-03	4.18E-03	4.53E-03	4.42E-03	4.21E-03
Trial 2	3.50E-03	3.62E-03	5.00E-03	3.91E-03	4.36E-03
Trial 3	4.66E-03	3.91E-03	4.36E-03	4.64E-03	4.20E-03
Trail 4	4.04E-03	4.92E-03	4.68E-03	4.49E-03	4.03E-03
Trail 5	4.28E-03	4.76E-03	4.72E-03	4.16E-03	4.08E-03
Average	4.22E-03	4.28E-03	4.66E-03	4.32E-03	4.17E-03

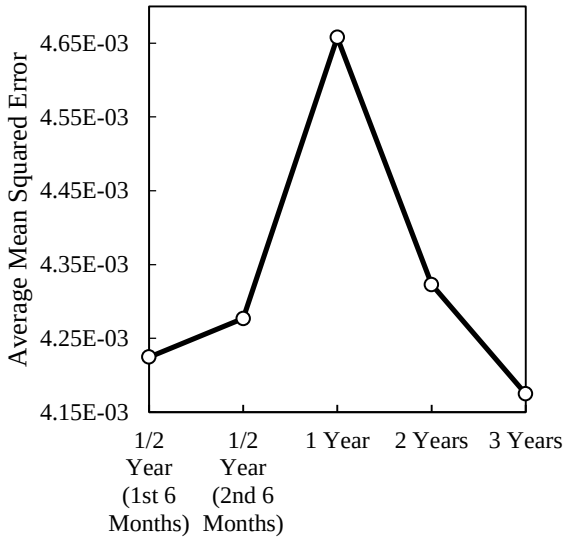

Figure 47: MSE of the Optimal Setup for Yearly Solar Irradiance Forecasting Graph

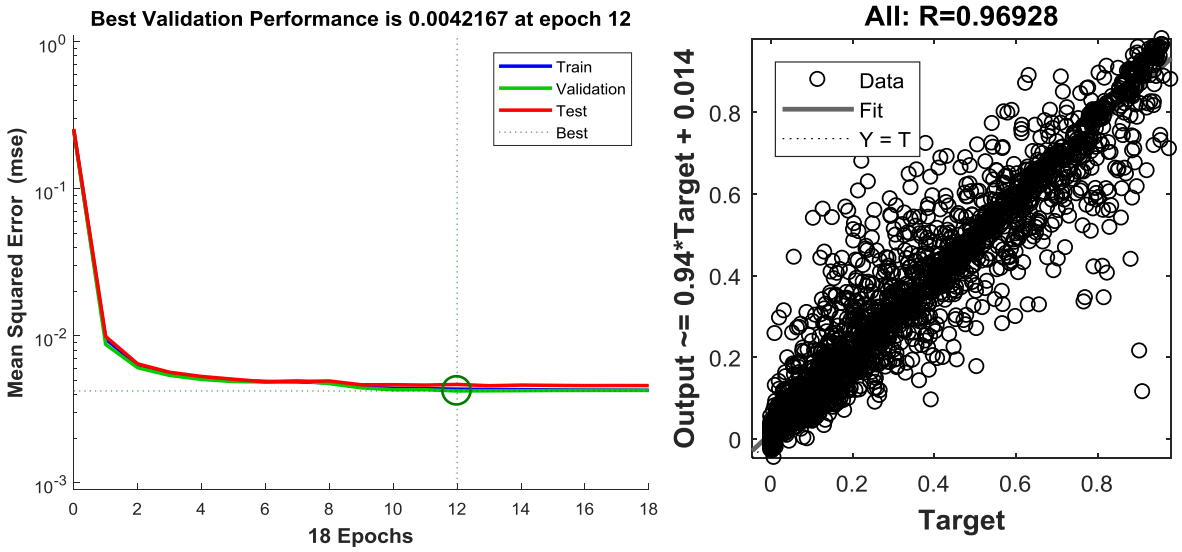

Figure 48: ½ Year (1st 6 Months) Validation Performance and Regression Values of the MSE for the Normalized Data of Colorado using the NARX Model

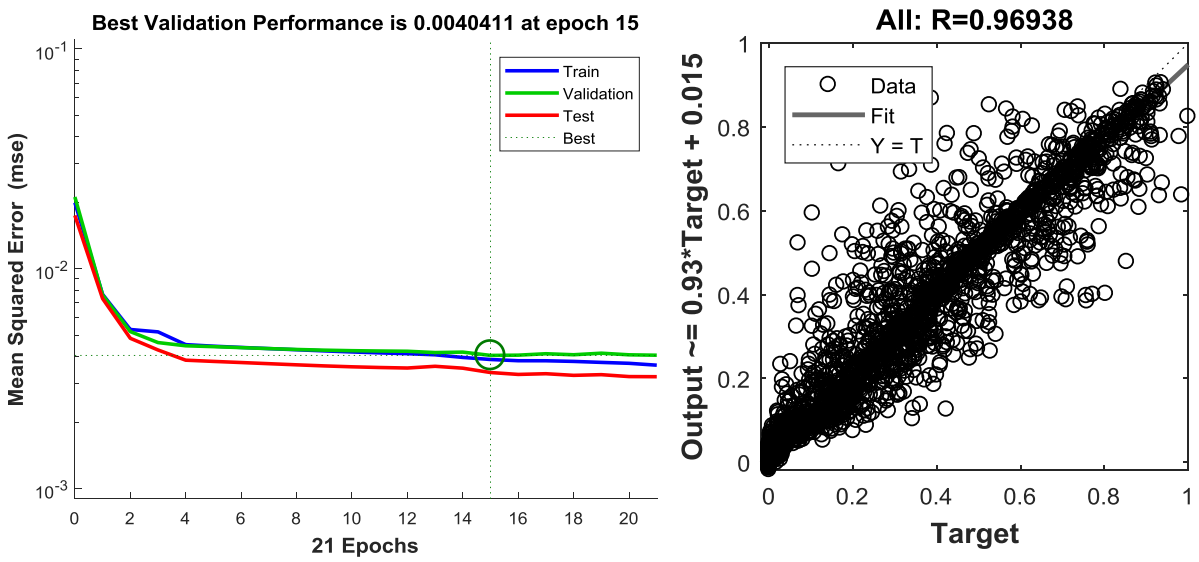

Figure 49: ½ Year (2nd 6 Months) Validation Performance and Regression Values of the MSE for the Normalized Data of Colorado using the NARX Model

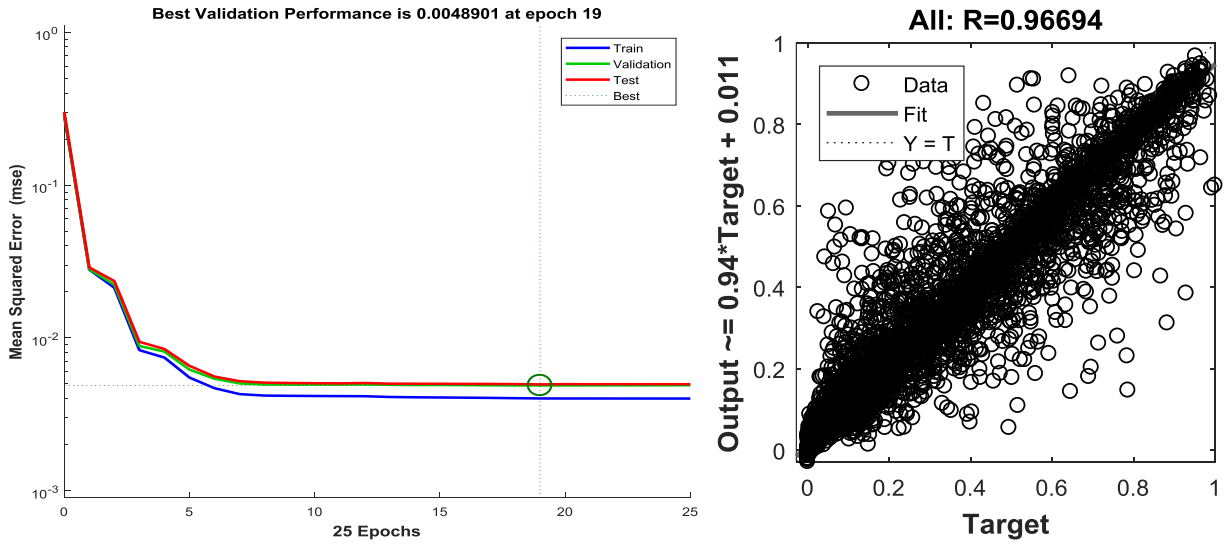

Figure 50: 1 Year Validation Performance and Regression Values of the MSE for the Normalized Data of Colorado using the NARX Model

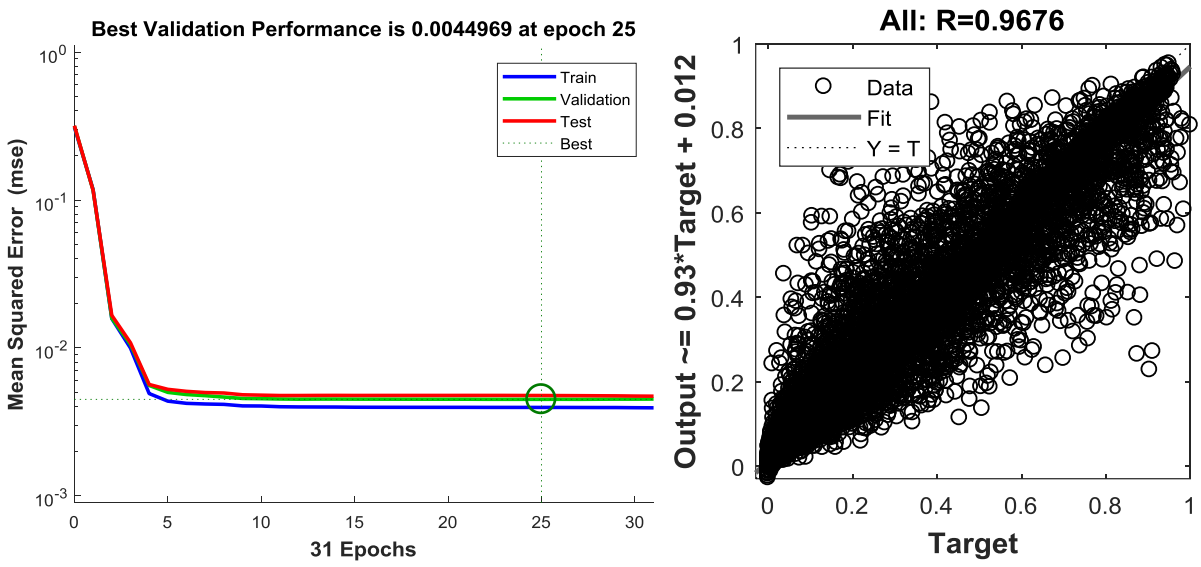

Figure 51: 2 Year Validation Performance and Regression Values of the MSE for the Normalized Data of Colorado using the NARX Model

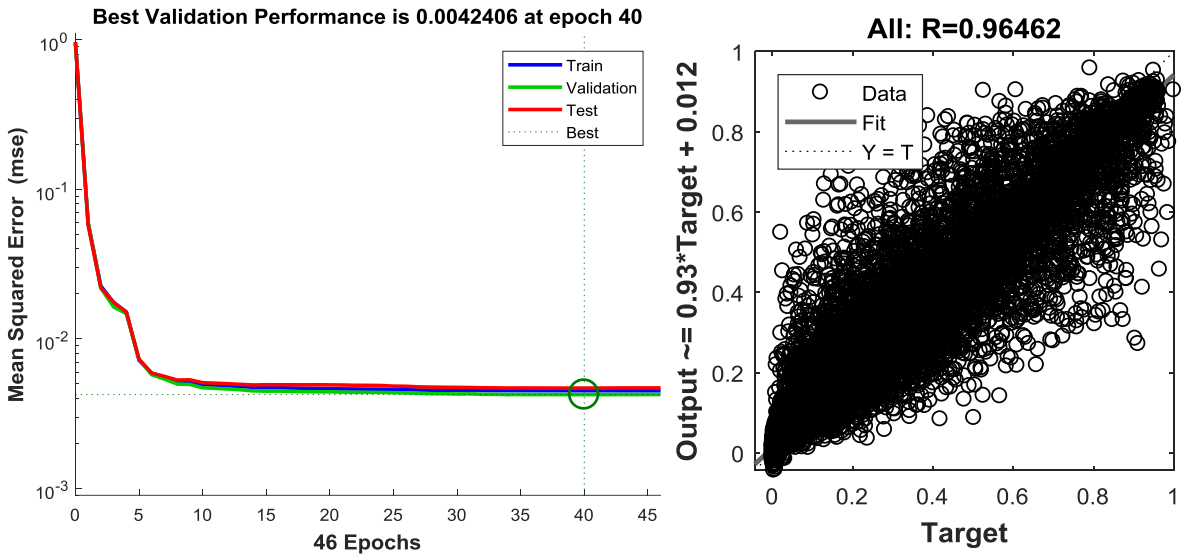

Figure 52: 3 Year Validation Performance and Regression Values of the Optimal for the Normalized Data of Colorado using the NARX Model

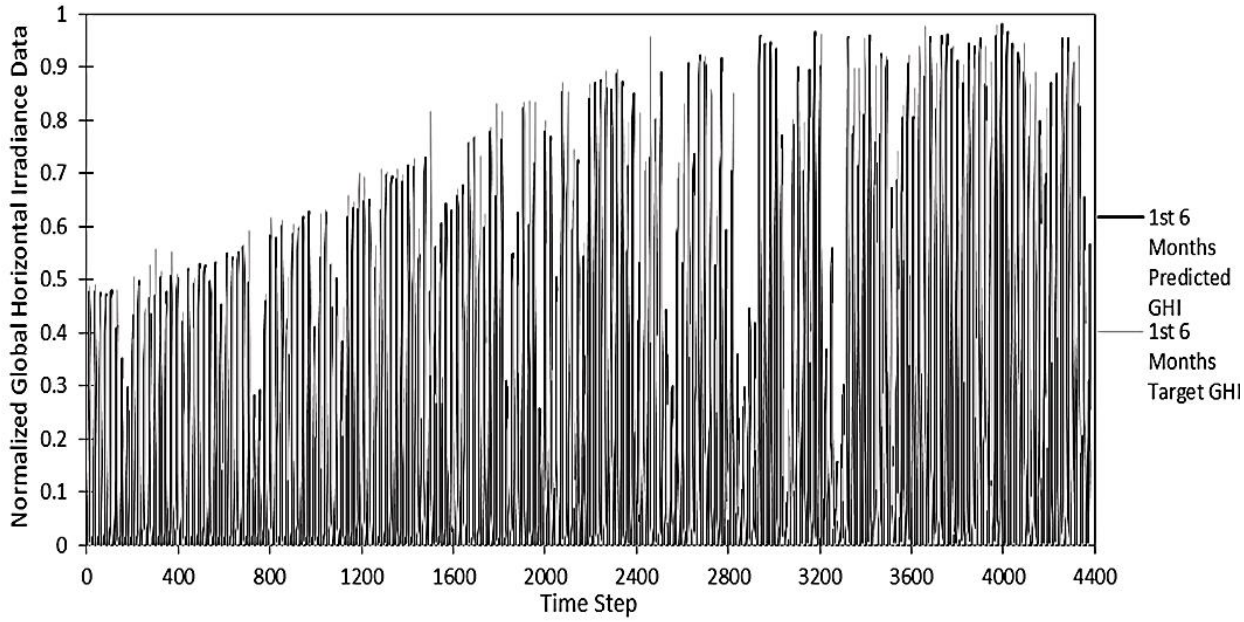

Figure 53: ½ Year (1st 6 Month) Global Horizontal Irradiance Single-Step Ahead Prediction Comparison of Target Values vs. Predicted

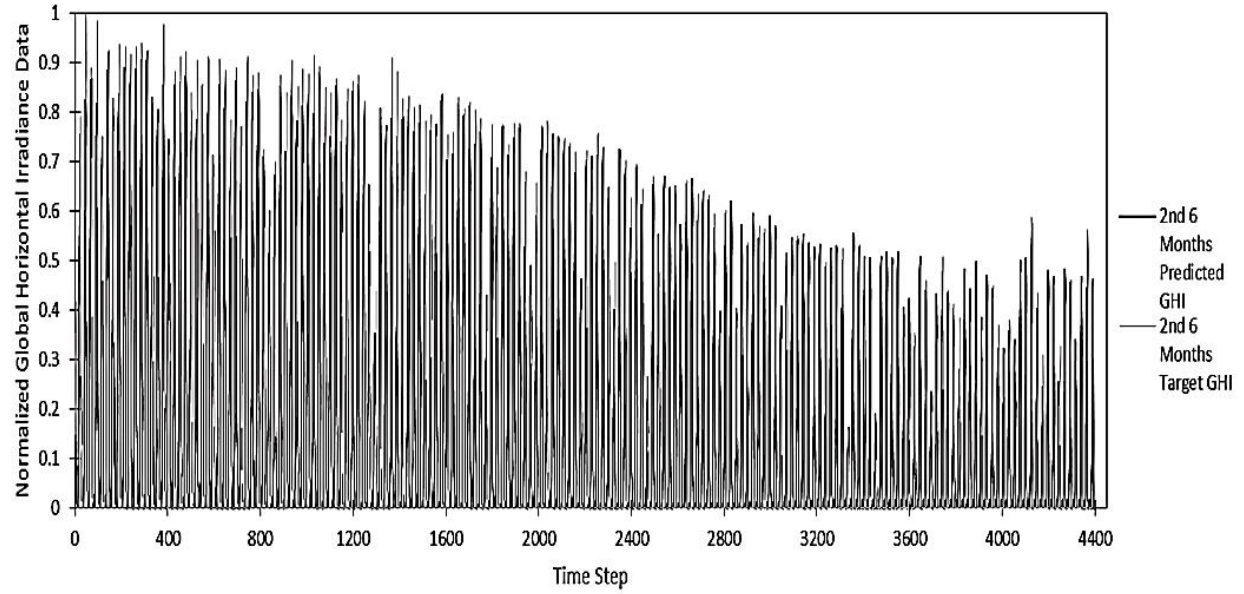

Figure 54: ½ Year (2nd 6 Month) Global Horizontal Irradiance Single-Step Ahead Prediction Comparison of Target Values vs. Predicted

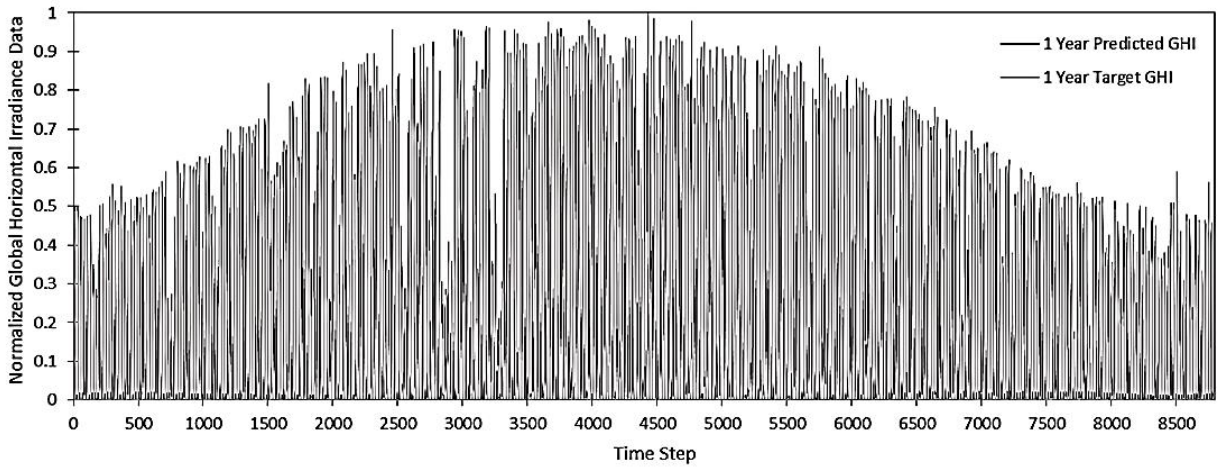

Figure 55: 1 Year Global Horizontal Irradiance Single-Step Ahead Prediction Comparison of Target Values vs. Predicted

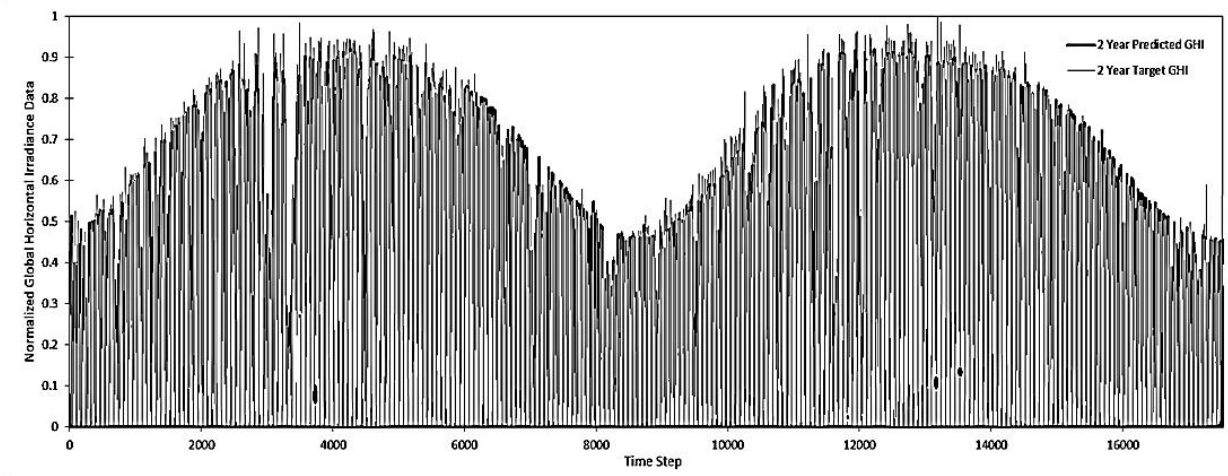

Figure 56: 2 Year Global Horizontal Irradiance Single-Step Ahead Prediction Comparison of Target Values vs. Predicted

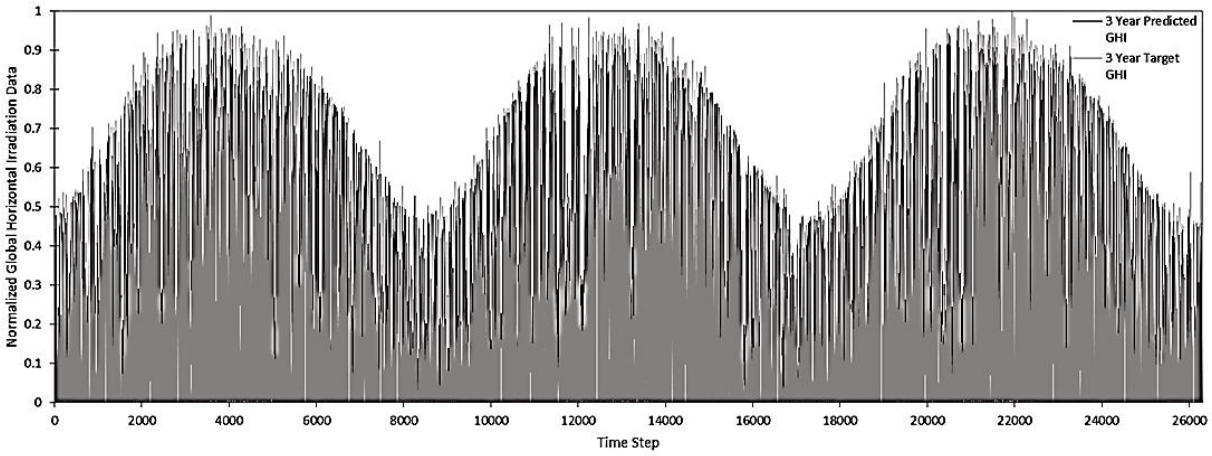

Figure 57: 3 Year Global Horizontal Irradiance Single-Step Ahead Prediction Comparison of Target Values vs. Predicted

Local Solar Irradiation Data Forecasting Results

As determined by the remote forecasting results, NARX networks produce reputable predictions while requiring less historical data. This provided the justification for utilizing less abundant local solar irradiance and meteorological data here at Georgia Southern University as the solar irradiance data ranged from Aug. 16, 2017 to Oct. 16, 2017 for prediction. Previous ANN modeling also determined that the hour of day, direct normal irradiance, diffuse horizontal irradiance, zenith angle, and azimuth angle provided suitable results as NARX network input parameters. Since cloud coverage percentage was not feasible locally, these exogenous inputs were utilized within the ANN of the local data set. The trail-and-error procedure was also used to determine the optimal delay parameters and number of neurons within the hidden layer.

Just as for the remote ANN model, the optimal delay parameter was determined by keeping number of neurons at the default value of 10. The delay parameters represent the number of hours the ANN utilized to execute the prediction. Nine different delay values were utilized to determine the optimal delay parameter. The delay values included: d = 1, 2, 3, 4, 5, 6, 8, 10, and 12. With the fixed number of neuron parameter, trial and error testing was done in order to

optimize the results. Table 8 and Figure 58 shows the average mean squared error (MSE) of five trials for each delay of the optimal model. Similarly to the remote ANN modeling procedure, the minimal amount of delays to produce the lowest MSE was 2 hours and the MSE continued to increase along with the delay values, so it is verified that solar irradiance data is more accurately predicted with a lower amount of feedback delays.

After the determination of the optimal amount of delays, that value was used to determine the optimal number of neurons.

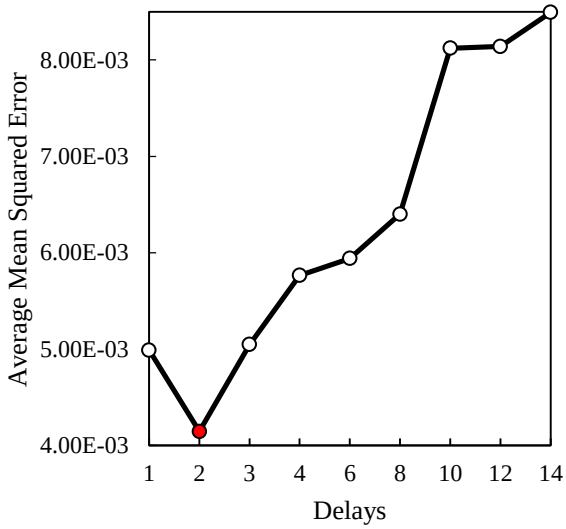

Figure 58: MSE of the Delay Parameter Obtained with the NARX Model of the Local Data Set Graph

Table 9 and Figure 59 depict the MSE for the different number of neurons utilized from a range of one to twelve. The value was increased until it was evident that the MSE was not improving, as drastic increases in the parameter will result an increase in local maximum and cause overtraining during the LM learning algorithm. From the table, it can be deduced that the optimal MSE values for the local data set also occurs at either four to five neurons in the hidden layer.

Table 8: MSE of the Delay Parameter Obtained with the NARX Model of the Local Data Set

	Number of Delay Parameter								
	1	2	3	4	6	8	10	12	14
Trial 1	5.50E-03	4.76E-03	5.70E-03	5.51E-03	5.57E-03	1.01E-02	1.07E-02	7.23E-03	7.73E-03
Trial 2	4.08E-03	4.76E-03	5.00E-03	6.14E-03	6.30E-03	5.10E-03	4.65E-03	6.52E-03	9.23E-03
Trial 3	5.78E-03	3.36E-03	5.40E-03	5.34E-03	6.11E-03	7.25E-03	1.15E-02	9.42E-03	8.25E-03
Trail 4	4.30E-03	4.84E-03	4.70E-03	6.58E-03	6.45E-03	4.86E-03	5.32E-03	8.37E-03	8.61E-03
Trail 5	5.29E-03	3.02E-03	4.44E-03	5.26E-03	5.27E-03	4.65E-03	8.43E-03	9.16E-03	8.64E-03
Avg.	4.99E-03	4.15E-03	5.05E-03	5.76E-03	5.94E-03	6.40E-03	8.12E-03	8.14E-03	8.49E-03

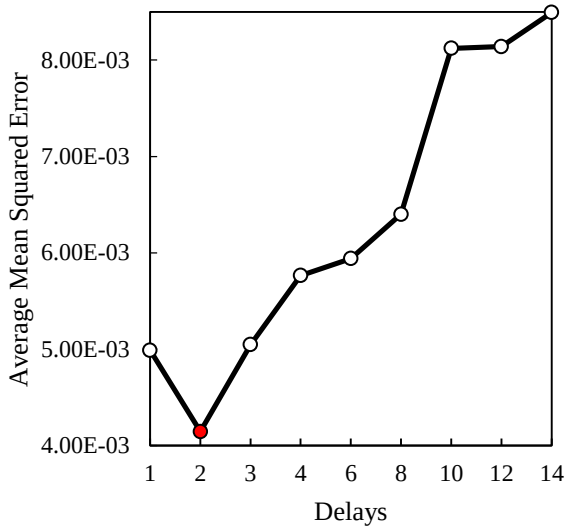

Figure 58: MSE of the Delay Parameter Obtained with the NARX Model of the Local Data Set Graph

Table 9: MSE of the Number of Neurons within the Hidden Layer Parameter Obtained with the NARX Model of the Local Data Set

	Number of Neurons within Hidden Layer								
	1	2	3	4	5	6	8	10	12
Trial 1	6.46E-03	5.63E-03	5.77E-03	5.35E-03	4.73E-03	4.11E-03	6.32E-03	5.98E-03	5.17E-03
Trial 2	9.92E-03	4.91E-03	4.30E-03	4.45E-03	3.88E-03	6.09E-03	6.40E-03	6.14E-03	5.45E-03
Trial 3	9.25E-03	7.91E-03	6.02E-03	4.04E-03	4.22E-03	5.73E-03	4.16E-03	5.61E-03	6.02E-03
Trail 4	5.40E-03	6.29E-03	4.66E-03	4.43E-03	4.25E-03	5.13E-03	4.97E-03	6.18E-03	6.26E-03
Trail 5	5.41E-03	6.40E-03	4.22E-03	3.63E-03	5.35E-03	5.02E-03	4.91E-03	4.29E-03	5.45E-03
Avg.	7.29E-03	6.23E-03	5.00E-03	4.38E-03	4.49E-03	5.22E-03	5.35E-03	5.64E-03	5.67E-03

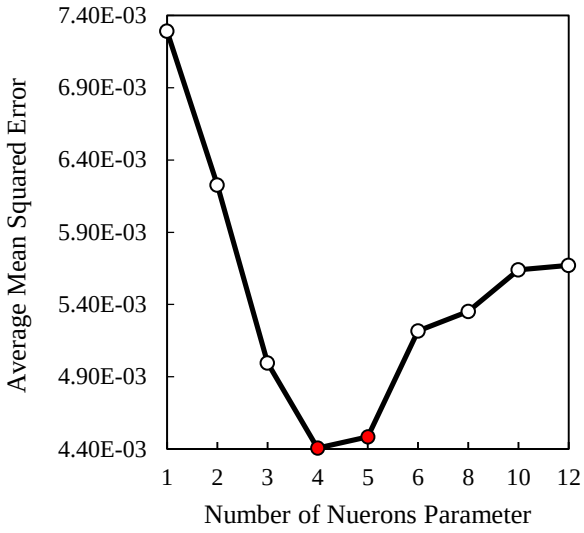

Figure 59: MSE of the Number of Neurons within the Hidden Layer Parameter

As seen in

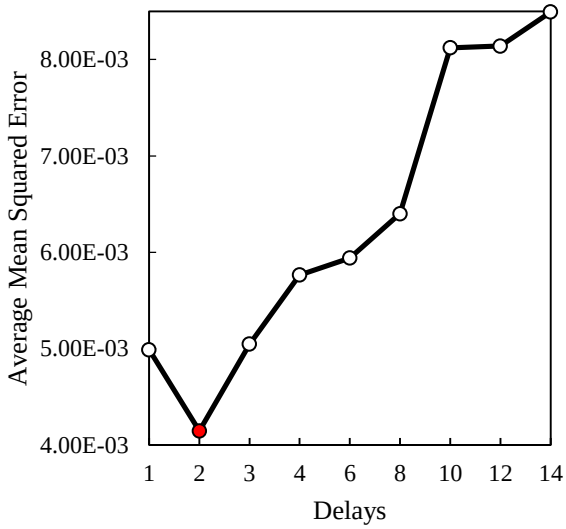

Figure 58: MSE of the Delay Parameter Obtained with the NARX Model of the Local Data Set Graph

Table 9, four neurons within the hidden layer produces the lowest MSE at 4.38E-03. So the optimal ANN model includes two feedback delays and four neurons within the hidden layer.

Figure 60 shows the best result of the optimal ANN for the local irradiance data. There was a validation performance of 0.003626 and a regression value of 0.96915.

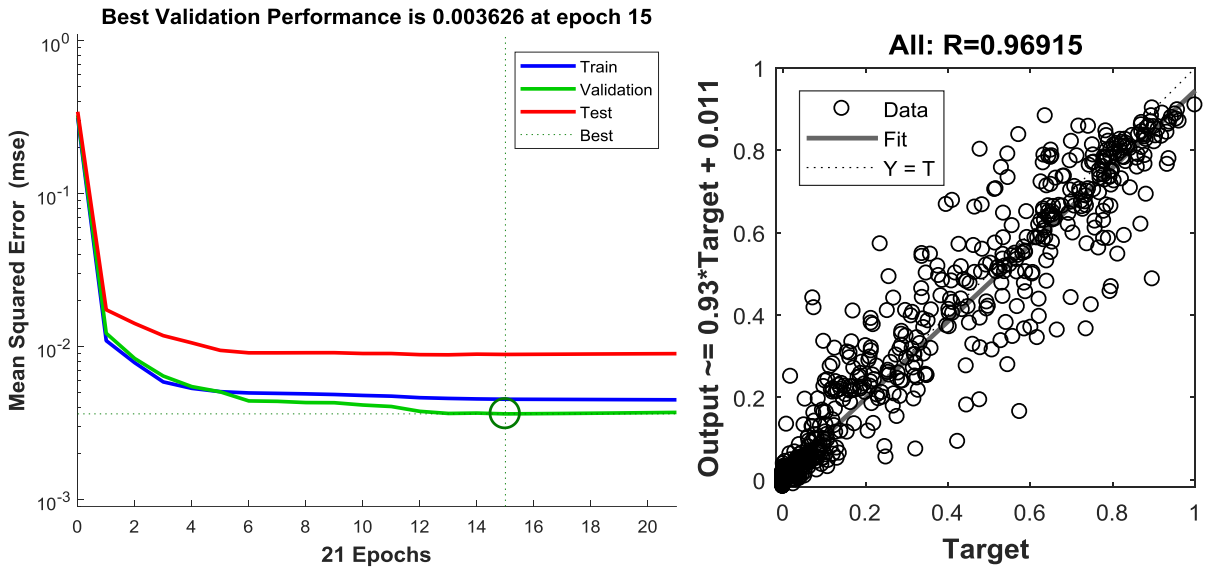

Figure 60: Validation Performance and Regression Values of the MSE for the Local Normalized Data using the Optimal NARX Model

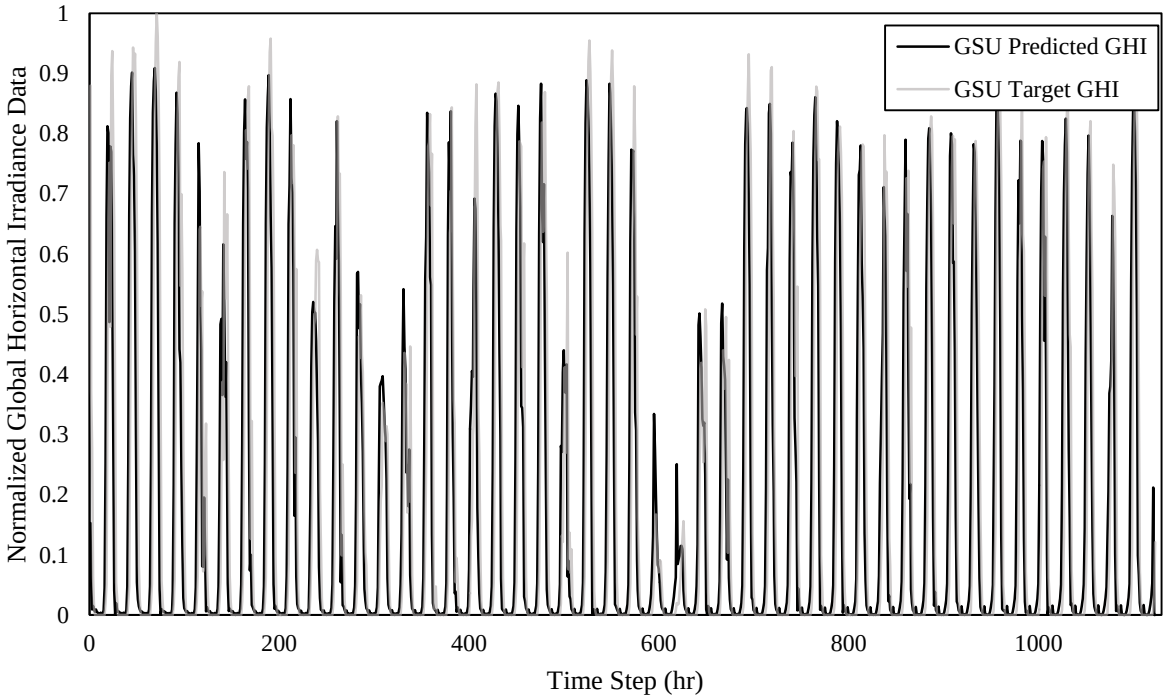

Figure 61: Local Normalized Global Horizontal Irradiance Single-Step Ahead Prediction

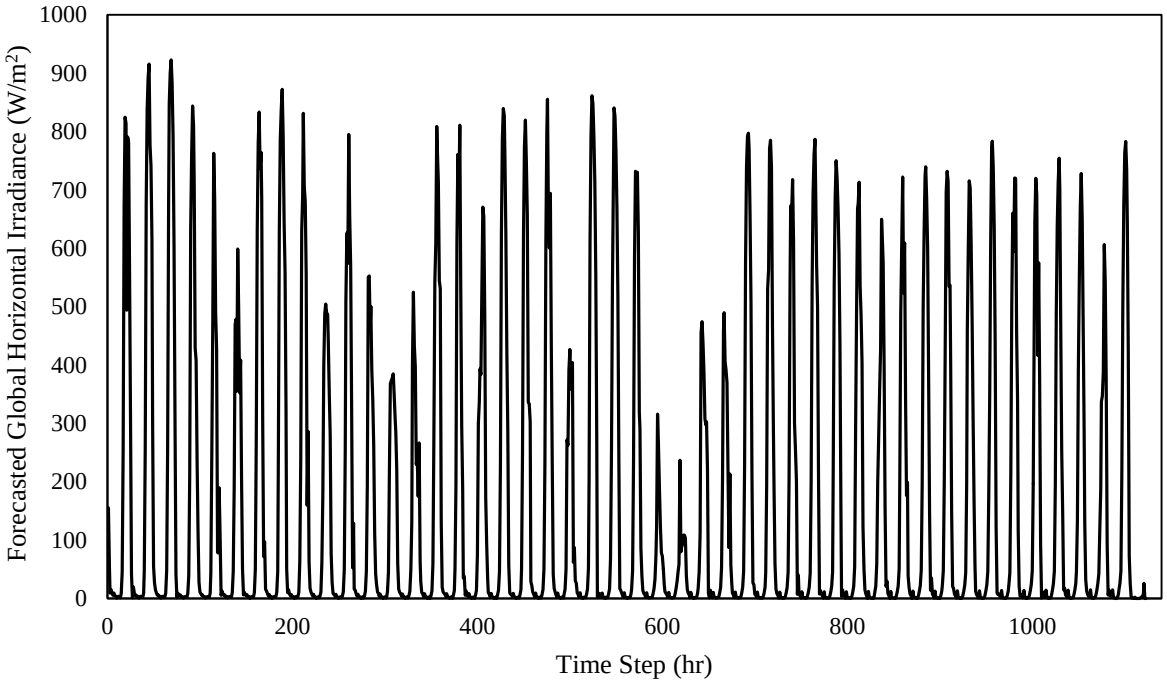

Figure 62: Local Denormalized Global Horizontal Irradiance Single-Step Ahead Prediction

Photovoltaic Modeling and Simulation Results

The photovoltaic module was modeled as if it were to be operating at the standard testing condition STC. The total current and voltage of the system were found according to varying solar irradiance values, and then the power vs voltage and current vs voltage of the system was determined by their values. Figure 63 represent the P-V characteristics graph that is determined by varying solar irradiance from 200 to $1000 W/m^2$. Figure 64 shows the I-V characteristics graph that is also determined by varying irradiance from 200 to $1000 W/m^2$.

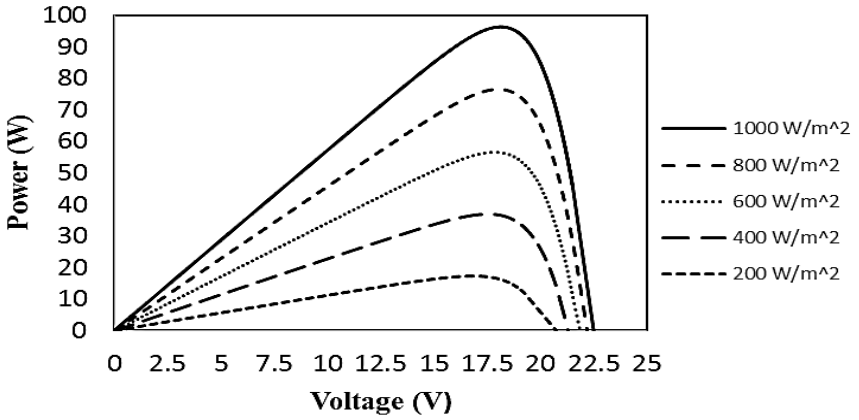

Figure 63: P-V Characteristics determined by Varying Irradiance

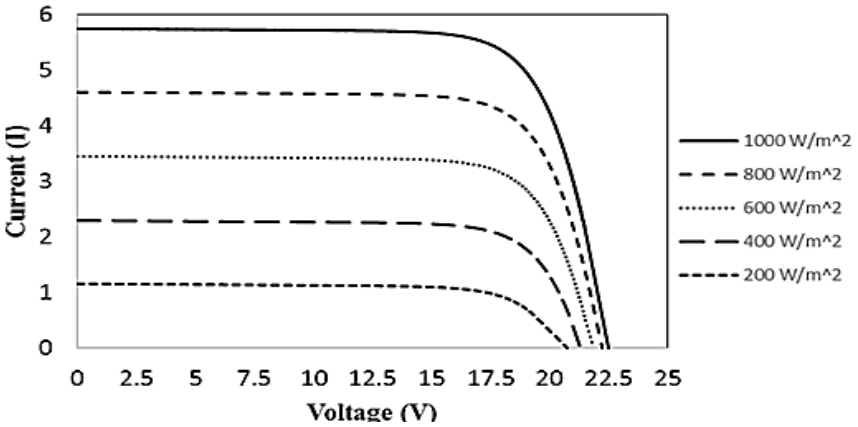

Figure 64: I-V Characteristic determined by Varying Irradiance

Table 10: Percent Error of the PV Model Characteristics vs PV Module Data Sheets

PV Model Characteristic	Value	Error (%)
P_{mp}	96.4 W	3.6
I_{mp}	5.31 A	0.39
V_{mp}	18.1 V	4.2
V_{oc}	22.3 V	0.89
I_{sc}	5.74 A	0.17

Concluding the modeling and simulation of the PV module, the results of 100 Watt PV model were implemented with the resulting predicted irradiance forecasting values from the ANN of

local data set and maximum power point tracking was used to determine the optimal PV output. These result (seen in Figure 65) is a representation of the potential output here at Georgia Southern University.

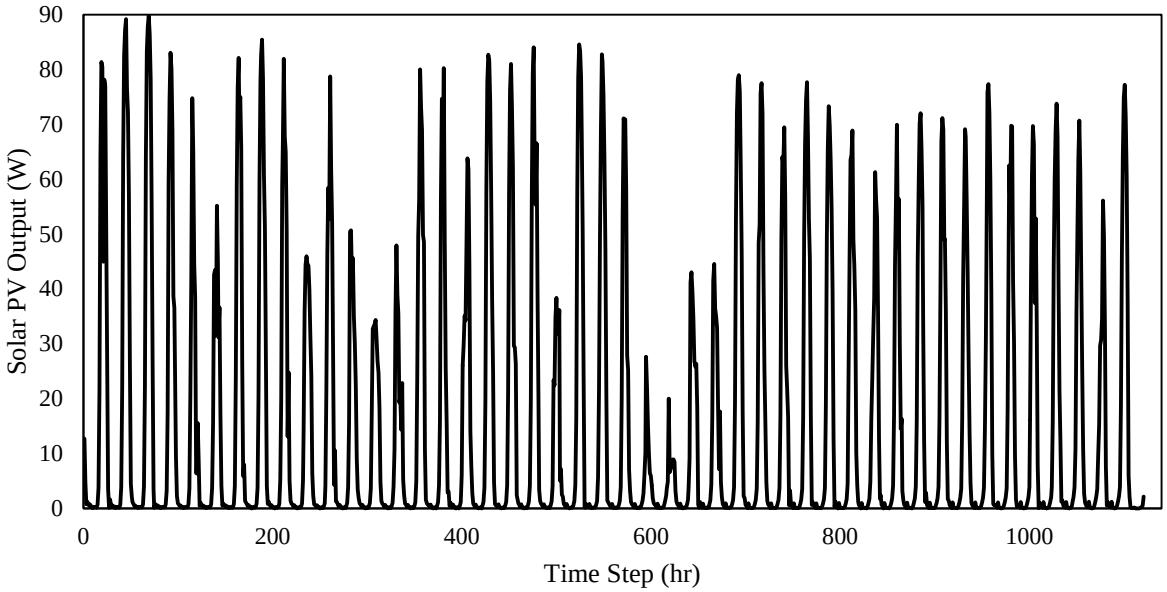

Figure 65: Local Predicted 100W Photovoltaic System Output (Aug. 16, 2017 – Oct. 16, 2017)

Domestic Electric Water Heater Modeling and PV Implementation Results

Since solar irradiance forecasting and PV modeling with implications of water heating is the ultimate goal, determining the potential output of this system is imperative. After determining the optimal production of the PV system. A 4×100 Watt PV array model was implemented into a domestic electric water heating model to display the on-grid dependencies of the typical DEWH and the PV inclusive DEWH. The systems were modeled to operate depending on an average typical hot water demand schedule [30]. The system was evaluated on a specific day (September 1, 2017) and the power demands compared.

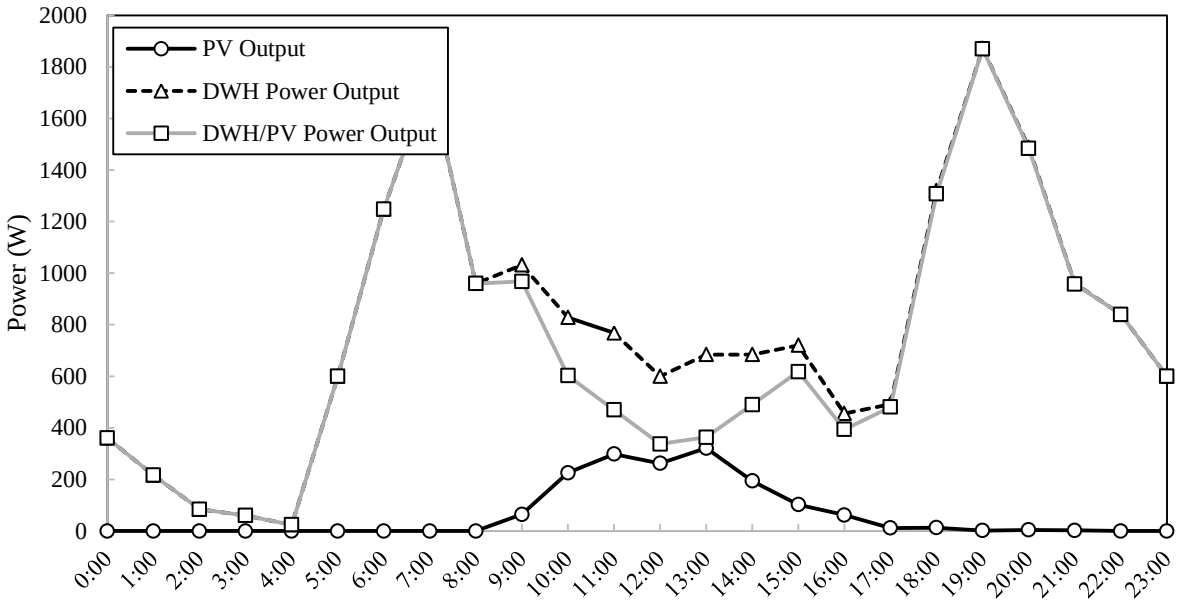

Figure 66: Typical DEWH vs PV Inclusive DEWH On-grid Dependency Comparison (September 1, 2017)

Discussion

This research concentrated on the forecasting of solar irradiance, PV modeling, and its implications for improving the energy efficiency of domestic electric water heaters. The first issue was considering which solar irradiance tracking equipment was reliable enough to provide accurate local (Georgia Southern University) solar irradiance data. Then it was important to determine the best location that has collected an extensive amount of data at the same accuracy. This is because the local solar irradiance data equipment was recently accumulated and installed, so the amount of historical data will increase accordingly with time. The Golden, Colorado's NREL Baseline Measurements Systems location was deemed to be the most reliable, because of its sole focus on meteorological and solar irradiance data. This remote solar irradiance data was used within the artificial neural networking methods to determine the proper configurations to produce the optimal model. These configurations were then applied to the local solar irradiance data to produce the same optimization. After optimizing the ANN for the local data set, the

potential local PV output was determined. That same PV module was connected to form an array and the results were added to a DEWH to predict the future on-grid dependency.

In terms of the remote (Golden, CO) data, the average mean squared errors of the six different input tests can be seen in Figure 31. Input configuration # 3, a NARX model produced the optimal results while including external inputs such as: hour of the day, direct normal irradiance, diffused horizontal irradiance, azimuth angles, zenith angles, and cloud coverage percentage. The NAR model, input configuration # 0, produced the least effective solution. Review of these results also shows that cloud coverage percentage is a valuable external input to solar irradiance prediction, but reputable results can be determined if it is unavailable. It also shows that historical external inputs like relative humidity and temperature don't necessarily relate to the prediction of global horizontal irradiance. In a majority of ANN problems, the result of a NARX network will be significantly better than that of a NAR network. Although, the results will falter if the external inputs don't necessarily relate to the target data.

Using the optimal NARX model, input configuration #3, the optimal delay parameters and number of neurons within the hidden layer was determined. From Figure 36, it was determined that a two hour feedback delay produced the optimal model and this was well within the realm of realistic solar irradiance prediction due to the potential variance of actual solar irradiance. Keeping the optimal delay parameter at two hours, the optimal number of neurons within the hidden layer was determined. Figure 37 represents the results of the number of neuron testing, and the optimal result was four neurons. As the amount of neurons were increased, the MSE gradually increased. This is due to the fact that as you increase this value the local maxima increases and the data can become over-fitted. Resulting this testing, optimal model required a two hour feedback delay and four hidden neurons within the hidden layer.

The optimal model was then used to focus on time dependent remote solar irradiance forecasting. These consisted of 4 season, ½ year, 1 year, 2 year, and 3 year solar irradiance data sets. This was done to determine what amount of data is necessary to optimally predict solar irradiance. Figure 38 represents the seasonal testing and it can be seen that the winter and fall results are considerably lower than the results of spring and summer. After a closer look at Figure 43 through Figure 46, it can be observed that the normalized data set for the winter and fall ranges from 0 to 0.8 as opposed to 0 to 1. This is due to the fact that there are lower irradiance values for these seasons because of the relative distance of the sun from the northern hemisphere and the duration of sunshine. This will reduce effect of skewing data results even more, ultimately, increasing the efficiency of these particular models. Also, the data set shows a gradual increase, as opposed to the varying values retrieved from the summer and spring seasons. In terms of yearly solar irradiance, shown in Figure 47, the two ½ year results produce very similar irradiance values. Observations of Figure 53 and Figure 54 shows that the targeted data also produced a gradual increase rather than producing extreme variance, so the pattern of the data is easier to predict. Figure 55 through Figure 57 represent the 1 year, 2 year, and 3 year results respectively, and as the amount of data increases, the average MSE of the model improves. This is due to the fact that the ANN will predict optimal results with more accumulation of historical data.

The results of the remote solar irradiance forecasting procedure proved that NARX networks are effective at predicting accurate results while requiring less historical data. So this served as justification of forecasting the local irradiance data retrieved here at Georgia Southern University. An ANN NARX model including the external inputs of the hour of day, direct normal irradiance, diffuse horizontal irradiance, zenith angle, and azimuth angle were used to

predict the results. Cloud coverage percentage wasn't included as an external input locally, because it isn't feasible currently. Although, remote results previously found that these external inputs can produce reputable results. The same procedure to determine remote delay parameter and number of neurons within the hidden layer was used locally. Figure 58 represents the results of the delay parameter testing, and it shows that the two hour feedback delay produced to optimal result. This value was then kept constant to determine the optimal amount of neurons. Figure 59 shows the results of the number of neurons within the hidden layer testing, and four neurons was determined to be the optimal number. Despite the inclusion of less data, the optimal model of the local data, with an average MSE of 4.38E-03, required the same amount of delay parameters and number of neurons as the remote data at an average MSE of 4.20E-03. This further validated to ability to properly forecast the local solar irradiance data. Figure 61 is the graphical representation of the comparison of the predicted local irradiance data to the target local irradiance data. The benefit of normalizing data set decreases the range of variance of the data set, but that same data set can be denormalized back to its original unit. Figure 62 represents the denormalized predicted local solar irradiance data.

After the determining of the local solar irradiance forecasting results, the PV panel model was evaluated according to varying solar irradiance. Figure 63 and Figure 64 represent the modeled characteristics of the PV module and

Table 10 depicts the percent error between the PV model and the physical module. The percent error for each characteristic was less than 5 percent, so the model is validated as a proper representation of the physical system. Figure 65 show the result of determining the potential local PV output according to the local predicted data. This result was then added to the DEWH for a specific day and it was determined that a PV inclusive water heater has the potential to

reduce the on-grid dependency of a typical DEWH operating of 18,648 Watts per day to 17,086.5 Watts per day. This resulted in an 8.38% decrease in on-grid dependency. Despite tremendous values for this particular day, these results are highly dependent on the solar irradiance and its resulting PV output. This model also doesn't take the potential use of battery storage and its benefits.

CHAPTER 5: CONCLUSION

This body of work described and tested the procedure of using artificial neural networks to forecast solar irradiance. This method collected hourly historical solar irradiance and meteorological information from Golden, Colorado (remote location) and Georgia Southern University (local location). As the local equipment is relatively new, it was important to determine how much irradiance data is needed to properly predict it. The data from both of these locations was normalized to be within a range of zero to one to reduce the skewing and to compare the results. For the remote data, different input configuration were tested to determine if NAR or NARX prediction models produced better results. Both presented reputable results, but ultimately NARX models were the optimal choice. More specifically, NARX models that included external inputs such as HOD, DNI, DHI, azimuth angle, zenith angle, cloud coverage percentage were the best fit for solar irradiance forecasting. After further optimization of the NARX model, it was determined that proper results could be determined using less historical data and this served as the justification needed to utilize ANN for the local solar irradiance forecasting. Similar ANN procedures were duplicated and results showed that local solar irradiance data is extremely reputable. After the extensive study of artificial neural network modeling of local solar irradiance data. A study was completed to determine the effects of a potential PV inclusive water heater. The local predicted solar irradiance data was used to determine potential PV output by presenting the predicted values in a PV simulated model. Those results were then model into a PV array and applied to the modeled operation of a domestic electric water heater. Comparisons of this system to that of a typical domestic electric water heater showed that a PV inclusive system could potentially decrease the on-grid dependency of the DEWH drastically.

REFERENCES

[1] S. Jabosson and A. Johnson, "The diffusion of reneable energy technology: an analytical framework and key issues for research," Gothenburg, 1998.

[2] U.S. Energy Information Administration, "U.S. Energy Consumption by Energy Source," 2016.

[3] "Global Warming Impacts: The consequences of climate change are already here.," 21 May 2016. [Online]. Available: http://www.ucsusa.org/our-work/global-warming/science-and-impacts/global-warming-impacts#.WA9sn_krKUk. [Accessed 4 October 2016].

[4] R. Matulka, "AskEnergySaver: Home Water Heating," Wahington DC, 2014.

[5] L. Cristaldi, M. Faifer, M. Rossi and F. Ponci, "A Simple Photovoltaic Panel Model: Characterization Procedure and Evaluation of the Role of EWnvironmental Measurements," *IEEE Transactions on Instrumentation and Measurement,* vol. 61, no. 10, p. 2632, 14 September 2012.

[6] B. J. Roberts, "Photovoltaic Resource of the United Staters," National Renewable Energy Laboratory, 201.

[7] N. Gilroy, "Direct Normal Solar Resource of Georgia," National Renewable Energy Laboratory, 2017.

[8] M. Diagne, M. David, P. Lauret, J. Boland and N. Schmutz, "Review of solar irradiance forecasting methods and a proposition for small-scale insular grids," *Renewable and*

Sustainable Energy Reviews, p. 65–76, 2013.

[9] G. Reikard, "Predicting solar radiation at high resolutions: A," *Solar Energy,* pp. 342-349, 2009.

[10] D. Heinemann, E. Lorenz and M. Girodo, "Forecasting of solar radiation based on satellite data," *EUROSUN2004 (ISES Europe Solar Congress,* pp. 223-233, 2006.

[11] T. H. Blanchard, "Wind Turbine Noise and Wind Speed Prediction," 2017.

[12] A. Sfetsos and A. H. Coonick, "Univariate and multivariate forecasting of hourly solar radiation with artificial intelligence techniques," *Solar Energy,* pp. 169-178, 2000.

[13] B. Amrouche and X. L. Pivert, "Artificial neural network based daily local forecasting for global solar radiation," *Applied Energy,* p. 333–341, 2014.

[14] H. A. B. Siddique, P. Xu and R. W. D. Doncker, "Parameter Extractiom Algorithm for One-Diode Model of PV Panels based on Datasheet Values," Aachen, Germany, 2013.

[15] D. Bonkoungou, Z. Koalaga and D. Njomo, "Modelling and Simulation of photovoltaic module considering single-diode equivalent circuit model in MATLAGB," *International Journal of Emerging Technologu and Advanced Engineering* , pp. 493-502, 2013.

[16] D. S. H. Chan and J. C. H. Phang, "Analytical Methods for the Extraction of Solar-Cell Single- and Double-Diode Model Paramters for I-V Characteristics," *IEEE Transactions on Electron Devices,* vol. 2, no. 34, pp. 286-293, 1987.

[17] K. Ishaque, Z. Salam and H. Taheri, "Simple, fast and accurate two-diode model for

photovoltaic modules," *Elsevier: Solar Energy Materials & Solar Cells,* pp. 586-594, 20 October 2011.

[18] K. Dezelak, P. Bracinik, M. Hoger and A. Otcenasova, "Comparison between the particle swarm optimisation and differential evolution approaches for the optimal proportional–integral controllers design during photovoltaic power plants modelling," *IET Renewable Power Generation,* pp. 522-530, 2015.

[19] Z. Salam, K. Ishaque and H. Taheri, "An Improved Two-Diode Photovoltaic (PV)," *Proc. Joint Int. Conf. Power Electron., Drives and Energy,* pp. 1-5, 2010.

[20] Y. Mahmoud, X. Xaio and H. H. Zeineldin, "A Simple Approach to Modeling and Simulation of Photovoltaic Modules," *IEEE TRANSACTIONS ON SUSTAINABLE ENERGY*, vol. 3, no. 1, pp. 185-186, January 2012.

[21] M. Taherbaneh, G. Farahani and K. Rahmani, "Evaluation the Accuracy of One-Diode and Two-Diode Models for a Solar Panel Bassed Open-Air Climate Measurements," in *Solar Cells - Silicon Wafer-Based Technologies*, vol. 4, L. A. Kosyachenko, Ed., InTech, 2011, pp. 201-228.

[22] M. A. Bregaw, "Modeling, Simulation and Optimization of Residential and Commercial Energy Systems," DuraSpace, Halifax, Nova Scotia, 2013.

[23] R. Diao, S. Lu, M. Elizondo, E. Mayhorn, Y. Zhang and N. Samaan, "Electric Water Heater Modeling and Control Strategies for Demand Response," in *IEEE Power and Energy Society General Meeting*, San Diego, 2012.

[24] Z. Xu, R. Diao, S. Lu, J. Lian and Y. Zhang, "Modeling of Electric Water Heaters for Demand Response: A Baseline PDE Model," *IEEE TRANSACTIONS ON SMART GRID*, pp. 2203-2210, 2014.

[25] H. M. Nehrir, R. Jia, D. A. Pierre and D. J. Hammerstrom, "Power management of Aggregate Electric Water Heater Loads by Voltage Control," *IEEE Power Eng. Soc*, p. 4275790, 2007.

[26] A. Andreas and T. Stoffel, "NREL Solar Radiation Research Laboratory (SRRL): Baseline Measurement System (BMS); Golden, Colorado (Data)," NREL, 1981.

[27] Mathworks, "Neural Network Toolbox: User's Guide (R2017a)," Mathworks, 2017.

[28] S. Islam, M. Kabir and N. Kabir, "Artificial neural networks based prediction of insolation on horizontal surfaces for Bangladesh," in *International Conference on Computational Intelligence: Modeling Techniques and Applications (CIMTA) 2013*, 2013.

[29] H. M. Pauzi and L. Abdullah, "Neural Network Training Algorithm for Carbon Dioxide Neural Network Training Algorithm for Carbon Dioxide," in *Advanced Computer and Communication Engineering Technology*, 2014.

[30] B. Hendron, J. Burch and G. Barker, *Tool for Generating Realistic Residential Hot Water Event Schedules*, Golden, CO: National Renewable Energy Lab (NREL), 2010.

[31] J. B. Rawlings, "Tutorial Overview of Model Predictive Control," *IEEE Control Systems Magazine*, pp. 38-52, June 2000.

[32] Y. Zong, L. Mihet-Popa, D. Kullmann, A. Thavlov, O. Gehrke and H. W. Binder, "Model Predictive Controller for Active Demand Side Management with PV Self-consumption in," *IEEE PES Innovative Smart Grid Technologies Europe (ISGT Europe)*, pp. 1-8, 2013.

[33] D. Q. Mayne, J. B. Rawlings, C. V. Rao and P. O. M. Scokaert, "Constrained model predictive control: Stability and optimality," *Automatica*, vol. 36, no. 6, pp. 789-814, June 2000.

[34] S. Shongwe and M. Hanif, "Coparative Analysis of Different Single-Diode PV Modeling Methods," *IEEE Journal of Photovoltaics,* vol. 5, no. 3, pp. 938-945, 17 April 2015.

[35] C. L. Wadhwa, Generation, Distribution and Utilization of Electrical Energy, New Age International, 1989, p. 367.

[36] R. F. Halvgaard, J. B. Jorgensen, N. K. Poulsen and H. Madsen, "Model Predictive Control for Smart Energy System," DTU Compute PHD-2014; No. 327, Kongens Lyngby, 2014.

[37] F. Yang, Q. Sun, Q.-L. Han and Z. Wu, "Cooperative Model Prediction for Distributed Photovoltaic Power Generation Systems," *IEEE Journal of Emerging and Selected Topics in Power Electronics*, vol. 4, no. 2, pp. 412-420, June 2016.

[38] "IEEE Recommended Practice for Utility Interface of Photovoltaic (PV) Systems," *IEEE Standard 929-2000*, January 2000.

[39] F. Sossan, A. M. Kosek, S. Martinenas, M. Marinelli and H. Bindner, "Scheduling of Domestic Water Heater Power Demand for Maximizing PV-Consumtion Using Model Predictive Control," *IEEE PES Innovative Smart Grid Technologies Europe (ISGT Europe),*

pp. 1-5, 2013.

[40] *WATER HEATER TEST PROCEDURE RULEMAKING: DEVELOPMENT TESTING PRELIMINARY REPORT,* Washington : U.S. Department of Energy, 2006.

[41] J. Doe, "How to Write Bibliographies," *Adventure Works Monthly,* vol. III, no. 12, pp. 50-62, 2006.

[42] C. Cornwall, A. Horiuchi and C. Lehman, "Solar Geometry Calculator," 2017.

APPENDICES

Appendix A

Solar Equipment Configuration Code for the Campbell Scientific CR1000 Series Data Logger

```
'CR1000 Series Datalogger
'Campbell Scientific Inc.
'Kipp and Zonen
'Southern Georgia
'
'CR1000-NL120 -> LN Data Collection every 5 minutes
'CR1000-Measure solar instruments once per second
'(1) CHP1 (IRR + 10K Therm) NOTE: program written assuming Rf = 1K
' serial number 140110, Sensitivity 8.06 calibrated 4/22/2014
'(2) CMP10'S
' serial numbers: 140672, Sensitivity 8.65 calibrated 4/29/2014
' serial numbers: 140673, Sensitivity 9.04 calibrated 4/29/2014
'(2) CVF3'S -> Fans on continuously. 5W Heater on daily 5AM-7AM CST
    'Below is for future instreumnts
    '(1) CGR4 (IRR + 10K Therm) NOTE: program written assuming Rf = 1K
    'CR1000-Control 5W Power to Heaters via solid state relay

Public PTemp : Units PTemp = c
Public Batt_Volt : Units Batt_Volt = V
Public rTime(9) : Alias rTime(1) = {Year,Month,DOM,Hour,Minute,Second,uSecond,WeekDay,Day_of_Year}

Public CHP1     : Units CHP1 = W/m^2    : Alias CHP1 = DNI       : Const CHP1_Sens = 8.06
Public CHP1_Temp : Units CHP1_Temp = DegC
Dim V1_Vx_CHP1 : Dim Rs_CHP1 : Const Rf_CHP1 = 1000  '1.0000 K
Public CMP10_1  : Units CMP10_1 = W/m^2 : Alias CMP10_1 = GLOBAL : Const CMP10_Sens_1 = 8.65
Public CMP10_2  : Units CMP10_2 = W/m^2 : Alias CMP10_2 = DIFF   : Const CMP10_Sens_2 = 9.04

    Public CGR4      : Units CGR4 = W/m^2    : Alias CGR4 = IR        : Const CGR4_Sens = 11.56
    Public CGR4_Temp : Units CGR4_Temp = DegC
      Public CGR4_KTemp
      Public CGR4_K4Temp
```

```
      Public CGR4_Corr

     Dim V1_Vx_CGR4 : Dim Rs_CGR4 : Const Rf_CGR4 = 1000
    ' Public TRHData(2) : Units AirTC=Deg C: Units RH=%
    ' Alias TRHData(1)=AirTC : Alias TRHData(2)=RH
    ' Public BP_mmHg : Units BP_mmHg=mmHg

' Tachometer wired to Pulse Port 1
' Public CVF4_Speed
Public CVF4_Fan_Global_Spd : Units CVF4_Fan_Global_Spd = Hz
Public CVF4_Fan_DIFF_Spd : Units CVF4_Fan_DIFF_Spd = Hz
Public CVF4_Heater_Status

 Const Rf = 1000
Const a = 1.0295*10^-3
Const b = 2.391*10^-4
Const c = 1.568*10^-7

Const high = true : Const low = false

DataTable (OneMin,1,-1)
  DataInterval (0,1,Min,10)
  Minimum (1,Batt_Volt,FP2,False,False)
  Average (1,DNI,FP2,False)
  StdDev (1,DNI,FP2,False)
  Average (1,CHP1_Temp,FP2,False)
  StdDev (1,CHP1_Temp,FP2,False)
  Average (1,GLOBAL,FP2,False)
  StdDev (1,GLOBAL,FP2,False)
  Average (1,DIFF,FP2,False)
  StdDev (1,DIFF,FP2,False)

  Sample (1,CVF4_Fan_Global_Spd,FP2)
  Sample (1,CVF4_Fan_DIFF_Spd,FP2)
  Sample ( 1,CVF4_Heater_Status,FP2 )
```

```
      Average (1,IR,IEEE4,False)
      StdDev (1,IR,IEEE4,False)
      Average (1,CGR4_Temp,IEEE4,False)
      StdDev (1,CGR4_Temp,IEEE4,False)
      Average (1,CGR4_Corr,IEEE4,False)
      StdDev (1,CGR4_Corr,IEEE4,False)
    ' Average (1,AirTC,FP2,False)
    ' StdDev (1,AirTC,FP2,False)
    ' Sample (1,RH,FP2)
    ' Sample (1,BP_mmHg,FP2)
EndTable

DataTable (OneHr,1,-1)
  DataInterval (0,1,Hr,10)
  Minimum (1,Batt_Volt,FP2,False,False)
  Average (1,DNI,FP2,False)
  StdDev (1,DNI,FP2,False)
  Average (1,CHP1_Temp,FP2,False)
  StdDev (1,CHP1_Temp,FP2,False)
  Average (1,GLOBAL,FP2,False)
  StdDev (1,GLOBAL,FP2,False)
  Average (1,DIFF,FP2,False)
  StdDev (1,DIFF,FP2,False)

  Sample (1,CVF4_Fan_Global_Spd,FP2)
  Sample (1,CVF4_Fan_DIFF_Spd,FP2)
  Sample ( 1,CVF4_Heater_Status,FP2 )

      Average (1,IR,FP2,False)
      StdDev (1,IR,FP2,False)
      Average (1,CGR4_Temp,FP2,False)
      StdDev (1,CGR4_Temp,FP2,False)
    ' Average (1,AirTC,FP2,False)
    ' StdDev (1,AirTC,FP2,False)
    ' Sample (1,RH,FP2)
    ' Sample (1,BP_mmHg,FP2)
EndTable
```

```
'Main Program
BeginProg
  Scan (1,Sec,0,0)
    RealTime (rTime)
    PanelTemp (PTemp,_60Hz)
    Battery (Batt_Volt)

    'CHP1 Pyrheliometer DNI
    VoltDiff (DNI,1,mV25C,1,True ,0,_60Hz,1000/CHP1_Sens,0)
    'CHP1 Pyrheliometer Temperature (10K)
    BrHalf (V1_Vx_CHP1,1,Autorange,3,Vx1,1,2500,True ,0,_60Hz,1.0,0)
    Rs_CHP1 = Rf_CHP1*((V1_Vx_CHP1)/(1-V1_Vx_CHP1))
    CHP1_Temp=(a+(b*(LN(Rs_CHP1))+c*(LN(Rs_CHP1))^3))^-1 - 273.15

    'CHP10_1 (GLOBAL)
    VoltDiff (CMP10_1,1,mV25C,3,True ,0,_60Hz,1000/CMP10_Sens_1,0)

    'CHP10_2 (DIFF)
    VoltDiff (CMP10_2,1,mV25C,4,True ,0,_60Hz,1000/CMP10_Sens_2,0)

   'CVF4_FaN (PULSE)
   ' The nominal speed is 4400 rpm, resulting in 8800 pulses per minute
   ' which equals 146 Hz on the tacho output.
    PulseCount (CVF4_Fan_Global_Spd,1,1,0,1,1.0,0)
    PulseCount (  CVF4_Fan_DIFF_Spd,1,2,0,1,1.0,0)
    PortGet (CVF4_Heater_Status,1)

       'Test  CGR3 w/ 10K Thermistor
'    VoltDiff (CGR4,1,mV7_5,5,True ,0,_60Hz,1000/CGR4_Sens,0)
'    BrHalf (V1_Vx_CGR4,1,Autorange,11,Vx2,1,2500,True ,0,_60Hz,1.0,0)
'    Rs_CGR4 = Rf_CGR4*((V1_Vx_CGR4)/(1-V1_Vx_CGR4)
'    CGR4_Temp=(a+(b*(LN(Rs_CGR4))+c*(LN(Rs_CGR4))^3))^-1 - 273.15

       ' CGR4 (IR)
       VoltDiff (CGR4,1,mV25C,5,True ,0,_60Hz,1000/CGR4_Sens,0)
```

```
      '  CGR4 IR Temperature (10K)
        BrHalf (V1_Vx_CGR4,1,Autorange,11,Vx2,1,2500,True ,0,_60Hz,1.0,0)
        Rs_CGR4 = Rf_CGR4*((V1_Vx_CGR4)/(1-V1_Vx_CGR4))
        CGR4_Temp=(a+(b*(LN(Rs_CGR4))+c*(LN(Rs_CGR4))^3))^-1 - 273.15

    CGR4_Temp=(a+(b*(LN(Rs_CGR4))+c*(LN(Rs_CGR4))^3))^-1
    CGR4_KTemp=1/(a+(b*LN(Rs_CGR4))+c*(LN(Rs_CGR4))^3)
    CGR4_Corr = CGR4+5.67e-8*CGR4_KTemp^4
    CGR4_K4Temp=CGR4_KTemp^4

        'CS215 Temperature & Relative Humidity Sensor measurements AirTC and RH
        'SDI12Recorder(TRHData(),7,"0","M!",1,0)
        'CS106 Barometric Pressure Sensor measurement BP_mmHg
        'PortSet(1,1)
        'VoltSe(BP_mmHg,1,mV2500,12,1,0,_60Hz,0.240,500)
        'BP_mmHg=BP_mmHg*0.75006

        'Fan On Continuously
        'If Batt_Volt >= 11.0 Then
        '  PortSet(2,1)
        'Else
        '  PortSet(2,0)
        'EndIf

     'Heater On between 5AM and 7AM Daily
     If Hour >= 5 AND Hour < 7 AND Batt_Volt >= 11.5 Then
       PortSet (1,1)
     Else
       PortSet(1,0)
     EndIf

     CallTable OneMin
     CallTable OneHr

   NextScan
EndProg
```

Appendix B

Software Implementation of NAR Network in MATLAB R2017a

```
% Solve an Autoregression Time-Series Problem with a NAR Neural Network
% Script generated by Neural Time Series app
% Created 01-Nov-2017 23:37:48
%
% This script assumes this variable is defined:
%
%   COOutputs - feedback time series.

T = tonndata(COOutputs,false,false);

% Choose a Training Function
% For a list of all training functions type: help nntrain
% 'trainlm' is usually fastest.
% 'trainbr' takes longer but may be better for challenging problems.
% 'trainscg' uses less memory. Suitable in low memory situations.
trainFcn = 'trainlm';  % Levenberg-Marquardt backpropagation.

% Create a Nonlinear Autoregressive Network
feedbackDelays = 1:2;
hiddenLayerSize = 10;
net = narnet(feedbackDelays,hiddenLayerSize,'open',trainFcn);

% Prepare the Data for Training and Simulation
% The function PREPARETS prepares timeseries data for a particular network,
% shifting time by the minimum amount to fill input states and layer
% states. Using PREPARETS allows you to keep your original time series data
% unchanged, while easily customizing it for networks with differing
% numbers of delays, with open loop or closed loop feedback modes.
[x,xi,ai,t] = preparets(net,{},{},T);

% Setup Division of Data for Training, Validation, Testing
net.divideParam.trainRatio = 70/100;
net.divideParam.valRatio = 15/100;
net.divideParam.testRatio = 15/100;

% Train the Network
[net,tr] = train(net,x,t,xi,ai);

% Test the Network
y = net(x,xi,ai);
e = gsubtract(t,y);
performance = perform(net,t,y)

% View the Network
view(net)

% Plots
% Uncomment these lines to enable various plots.
%figure, plotperform(tr)
%figure, plottrainstate(tr)
%figure, ploterrhist(e)
```

```
%figure, plotregression(t,y)
%figure, plotresponse(t,y)
%figure, ploterrcorr(e)
%figure, plotinerrcorr(x,e)

% Closed Loop Network
% Use this network to do multi-step prediction.
% The function CLOSELOOP replaces the feedback input with a direct
% connection from the outout layer.
netc = closeloop(net);
netc.name = [net.name ' - Closed Loop'];
view(netc)
[xc,xic,aic,tc] = preparets(netc,{},{},T);
yc = netc(xc,xic,aic);
closedLoopPerformance = perform(net,tc,yc)

% Step-Ahead Prediction Network
% For some applications it helps to get the prediction a timestep early.
% The original network returns predicted y(t+1) at the same time it is
% given y(t+1). For some applications such as decision making, it would
% help to have predicted y(t+1) once y(t) is available, but before the
% actual y(t+1) occurs. The network can be made to return its output a
% timestep early by removing one delay so that its minimal tap delay is now
% 0 instead of 1. The new network returns the same outputs as the original
% network, but outputs are shifted left one timestep.
nets = removedelay(net);
nets.name = [net.name ' - Predict One Step Ahead'];
view(nets)
[xs,xis,ais,ts] = preparets(nets,{},{},T);
ys = nets(xs,xis,ais);
stepAheadPerformance = perform(nets,ts,ys)
```

Appendix C

Software Implementation of NARX Network in MATLAB R2017a

```
Solve an Autoregression Problem with External Input with a NARX Neural
Network
% Script generated by Neural Time Series app
% Created 02-Nov-2017 14:02:15
%
% This script assumes these variables are defined:
%
%   COInputs3 - input time series.
%   COOutputs - feedback time series.

X = tonndata(COInputs3,false,false);
T = tonndata(COOutputs,false,false);

% Choose a Training Function
% For a list of all training functions type: help nntrain
% 'trainlm' is usually fastest.
% 'trainbr' takes longer but may be better for challenging problems.
% 'trainscg' uses less memory. Suitable in low memory situations.
trainFcn = 'trainlm';  % Levenberg-Marquardt backpropagation.

% Create a Nonlinear Autoregressive Network with External Input
inputDelays = 1:2;
feedbackDelays = 1:2;
hiddenLayerSize = 10;
net = narxnet(inputDelays,feedbackDelays,hiddenLayerSize,'open',trainFcn);

% Prepare the Data for Training and Simulation
% The function PREPARETS prepares timeseries data for a particular network,
% shifting time by the minimum amount to fill input states and layer
% states. Using PREPARETS allows you to keep your original time series data
% unchanged, while easily customizing it for networks with differing
% numbers of delays, with open loop or closed loop feedback modes.
[x,xi,ai,t] = preparets(net,X,{},T);

% Setup Division of Data for Training, Validation, Testing
net.divideParam.trainRatio = 70/100;
net.divideParam.valRatio = 15/100;
net.divideParam.testRatio = 15/100;

% Train the Network
[net,tr] = train(net,x,t,xi,ai);

% Test the Network
y = net(x,xi,ai);
e = gsubtract(t,y);
performance = perform(net,t,y)

% View the Network
view(net)

% Plots
```

```
% Uncomment these lines to enable various plots.
%figure, plotperform(tr)
%figure, plottrainstate(tr)
%figure, ploterrhist(e)
%figure, plotregression(t,y)
%figure, plotresponse(t,y)
%figure, ploterrcorr(e)
%figure, plotinerrcorr(x,e)

% Closed Loop Network
% Use this network to do multi-step prediction.
% The function CLOSELOOP replaces the feedback input with a direct
% connection from the outout layer.
netc = closeloop(net);
netc.name = [net.name ' - Closed Loop'];
view(netc)
[xc,xic,aic,tc] = preparets(netc,X,{},T);
yc = netc(xc,xic,aic);
closedLoopPerformance = perform(net,tc,yc)

% Step-Ahead Prediction Network
% For some applications it helps to get the prediction a timestep early.
% The original network returns predicted y(t+1) at the same time it is
% given y(t+1). For some applications such as decision making, it would
% help to have predicted y(t+1) once y(t) is available, but before the
% actual y(t+1) occurs. The network can be made to return its output a
% timestep early by removing one delay so that its minimal tap delay is now
% 0 instead of 1. The new network returns the same outputs as the original
% network, but outputs are shifted left one timestep.
nets = removedelay(net);
nets.name = [net.name ' - Predict One Step Ahead'];
view(nets)
[xs,xis,ais,ts] = preparets(nets,X,{},T);
ys = nets(xs,xis,ais);
stepAheadPerformance = perform(nets,ts,ys)
```